Molecular fluorinated cobalt phthalocyanine immobilized on ordered mesoporous carbon as an electrochemical sensing platform for sensitive detection of hydrogen peroxide and hydrazine in alkaline medium.

YUAN, B., SUN, P., FERNANDEZ, C., WANG, H., GUAN, P., XU, H. and NIU, Y.

2022

.

Molecular fluorinated cobalt phthalocyanine immobilized on ordered mesoporous carbon as an electrochemical sensing platform for sensitive detection of hydrogen peroxide and hydrazine in alkaline medium

Baiqing Yuan [a, *], Peng Sun [a], Carlos Fernandez [b, *], Hemin Wang [a], Peiyu Guan [a], Hui Xu [c], Yuzhong Niu [a, *]

[a] School of Chemistry and Materials Science, Ludong University, Yantai 264025, Shandong, China

[b] School of Pharmacy and Life Sciences, Robert Gordon University, Garthdee Road, Aberdeen AB10 7GJ, United Kingdom

[c] College of Science and Engineering, Huzhou College, Huzhou 313000, China

*** Corresponding author.**

E-mail: baiqingyuan1981@126.com (B. Yuan); c.fernandez@rgu.ac.uk (C.Fernandez); niuyuzhong@ldu.edu.cn (Y, Niu)

Abstract:

Non-precious molecular cobalt phthalocyanine (CoPc) complexes have been considered to be promising electrocatalysts due to diversity of substituents and carbon supporting matrixes. Here, we report a highly dispersed fluorinated CoPc (CoPcF16) molecule electrocatalyst immobilized in ordered mesoporous carbon CMK-3 (CMK-3-CoPcF16) via π-π interaction. The molecular electrocatalyst is characterized by X-ray photoelectron spectroscopy, Raman spectrum, electronic paramagnetic resonance, scanning electron microscopy, transmission electron microscopy and electrochemical impedance spectroscopy. The combination of fluorine substituents and high loading capability of CMK-3 increase the solubility of CoPc, suppress aggregation, and thereby enhance the electrocatalytic performance. As a result, the CMK-3-CoPcF16 modified electrode shows high electrocatalytic activity towards the oxidation of hydrogen peroxide and hydrazine. CMK-3-CoPcF16 hybrid is successfully presented as an electrochemical sensing platform for sensitive detection of H_2O_2 and hydrazine with a detection limit of 0.03 and 0.2 μM, respectively.

Keywords: fluorinated cobalt phthalocyanine, ordered mesoporous carbon, hydrogen peroxide (H_2O_2), hydrazine, electrochemical sensors

1. Introduction

Metal phthalocyanines (MPc) are highly conjugated metal-N4 macrocyclic structures (a metal centre coordinated with four nitrogen atoms) and attract considerable attention as active components in electrocatalysis [1-3], electrochemical sensors [4, 5], photosensitisers [6] and modern organic electronic devices [7] due to their unique advantages in chemical stability and structural tunability. Pc can coordinate more than 70 elements of the periodic table. Though MPc are highly conjugated macrocycles, not all MPc are suitable to serve as an efficient electrocatalyst because their electronic properties depend on the central metal atom [8]. It is also found that the central metal atom of MPc is crucial for the presence of interfacial charge transfer [8].

Cobalt phthalocyanine (CoPc), a promising star of the MPc family, is well-studied in electrochemistry because of its intriguing electronic property [9], easy availability and low cost. Due to these properties, it is often employed as a dye at a large scale in the painting industry [10]. However, planar aromatic large structure of CoPc leads to self-assemble into stacks through π-π supramolecular interactions, and the inherent low solubility of pristine CoPc intensifies the aggregation, resulting in poor electron transport. Pristine CoPc are far from meeting the growing demands in electrocatalysis and electroanalysis where electrical conductivity and interfacial charge transport are emphasized. Fortunately, the structure of Pc macocycles can be modified by introducing peripheral (β) and non-peripheral (α) functional groups into the four corners of the benzene ring. The functionalities of CoPc macrocycle are related to the

electronic arrangement and electrocatalytic activity [11]. It has been well understood that electron-withdrawing substituents at the benzene rings of CoPc can activate the catalytic central Co ion toward electrochemical reactions [12, 13]. Peisert [14] recently investigated the interfacial properties of CoPc and fluorinated CoPc (CoPcF16) on conductive substrate. It was found that the central Co metal atom of CoPc and CoPcF16 on the interface behaved distinctly different, and a charge transfer to the Co ion is observed for CoPcF16 but not for CoPc. Kotresh first [5] studied the relationship between isomerism and the electrocatalytic activity of CoPc. The results showed that isomerism of functionality in the benzene rings of CoP independently contributed to electrocatalysis over their chemical identity [5, 11]. So far, many substituted CoPc have been molecularly anchored on different carbon materials for efficient electrocatalysis including β-NH_2-CoPc/CNT [1], trimethyl ammonium-tert-butyl-CoPc/CNT [15], Cyano-CoPc/CNT [16], CoNaPc/graphene [17], α-octaphenyl CoPc [18], octaalkoxy-CoPc/CNT [19], PolyCoPc/CNT [20], and Tetrakis (3-Trifluoromethylphenoxy)-CoPc/CNT [21].

Since the first report in 1999, ordered mesoporous carbon (OMC) has been of interest in many applications owing to their high surface area, well-defined pore size, electronic and ionic conductivities, as well as mechanical and thermal stabilities [22-26]. In this work, commercial available CoPcF16 with electron-withdrawing fluorine substituent and OMC CMK-3 were selected to construct molecular CoPc electrocatalyst via π-π interaction. This anchoring strategy allows catalytic molecules such as CoPcF16 to be highly dispersed on the surface of CMK-3 conductive

framework and renders molecular electrocatalysts. Compared with pristine CoPc, electron-withdrawing fluorine substituent of CoPcF16 increases the solubility and electrical conductivity. CMK-3 has a pore diameter of 3.8-4 nm which is larger than the size of square-planar CoPc complex (1.2 ×1.2 nm) [27]. CoPcF16 can be absorbed into/onto the pore of CMK-3 by strong π-π interactions to accomplish high surface coverage. The immobilized CoPcF16 exhibited molecular properties and avoid the aggregation, which was explored for the electrocatalytic reactions of hydrogen peroxide (H_2O_2) and hydrazine. The results showed that CMK-3-CoPcF16 modified electrode demonstrated high electrocatalytic activity, and sensitive detection of H_2O_2 and hydrazine was achieved.

2. Experimental

2.1. Chemicals and solutions

CoPcF16 were purchased from sigma Aldrich. H_2O_2 (wt. 30%) and hydrazine (wt. 80%) were acquired from Tianjin Damao Chemical Reagent Factory. CMK-3 was purchased from Nanjing XFNano Materials Tech Co., Ltd. All other chemicals were of analytical reagent grade and used without further purification. The aqueous solutions were prepared with doubly distilled water. 0.1 M NaOH solution was used as the background electrolyte.

2.2. Apparatus

The X-ray photoelectron spectroscopy (XPS) were recorded on a Thermo ESCALAB 250 Xi spectrometer fitted with a monochromatic Al Kα X-ray source. The morphologies were characterized by transmission electron microscopy (TEM)

(JEM-2100) and scanning electron microscopy (SEM) (Hitachi SU8010). The samples were also evaluated by Raman analysis (Renishaw inVia), and electronic paramagnetic resonance (EPR) (Bruker EMXPLUS). All the electrochemical experiments were carried out with a CHI 842C electrochemical workstation (Austin, TX, USA) with a conventional three-electrode system consisting of modified GCE working electrode, platinum coil auxiliary electrode, and Ag/AgCl (saturated KCl) reference electrode. The linear sweep voltammetry (LSV) measurements were conducted with ASL RRDE-3A equipment on the rotating ring-disk electrode (RRDE) (Pt ring, GCE disc: 4 mm) at a scan rate of 5 $mV \cdot s^{-1}$ in N_2 or O_2 saturated 0.1 M KOH solution.

2.3. Synthesis of CMK-3-CoPcF16 hybrid

Molecular CoPcF16 was anchored on CMK-3 via π-π interactions by mixing CoPcF16 and CMK-3 in DMF with the assistance of sonication. DMF is a suitable solvent for dissolving CoPcF16 and dispersing and CMK-3, allowing for immobilization of molecular CoPcF16 on CMK-3. 2 mg CMK-3 was ultrasonically dispersed in 4 mL DMF for 60 min. 4 mg CoPcF16 was dissolved in 4 mL DMF and kept at 60 ℃ for 60 min with the assistance of sonication, followed by centrifugation. The upper layer solution of CoPcF16 was added to CMK-3 dispersion, and the mixed suspension was sonicated for another 60 min. The prepared CoPcF16-CMK-3 hybrid was separated by centrifugation and washed several times with DMF and ethanol respectively, followed by drying to obtain the final product.

2.4 Electrode preparation and modification

Prior to modification, the GCE (3 mm diameter, 0.07 cm^2) was successively polished with 1, 0.3, and 0.05 μm alumina paste to a mirror finish and then rinsed with water followed by an ultrasonic treatment in water and ethanol, respectively. CoPcF16-CMK-3 modified GCE (CoPcF16-CMK-3/GCE) was prepared by dropping 5 μL ink from a CoPcF16-CMK-3/DMF suspension (0.3 mg/mL) on a cleaned GCE and kept to dry at room temperature. For control experiment, the CoPcF16/GCE and CMK-3/GCE were prepared by the same procedures. For preparation of CoPcF16-CMK-3 modified disk electrode, 3 mg of CoPcF16-CMK-3, 20 μL of 5 wt % nafion solution, 490 μL ethanol and 490 μL water were mixed and sonicated for 60 min to form a uniform catalyst ink. The GCE disc of RRDE was modified with the catalyst coverage of about 0.2 mg/cm^{-2}. The hydrogen peroxide yield (H_2O_2%) and electron transfer number n in ORR process can be calculated from the following equation:

$$H_2O_2\% = \frac{i_R/N_0}{i_D + i_R/N_0} \times 200\%$$

$$\mathrm{n} = 4 \times \frac{i_D}{i_D + i_R/N_0}$$

where i_D is the disk current, i_R is the ring current, and N_0 is the ring collection efficiency measured to be 0.401.

2.5. Sample analysis

Water samples from Yanjing lake at Ludong University were used without pretreatment for the practical sensing application of hydrazine.

3. Results and discussion

3.1. Characterization and electrochemical behavior of the modified electrodes

The molecular structure of CoPcF16 is illustrated in **Fig. S-1, Supplemental information.** The CoPcF16 molecule consists of four isoindole groups with fluorine substituents (F16) which are linked by four N_α nitrogen atoms to form a planar ring structure, and the metal atom (Co) is coordinated by four N_β in the center of the molecular ring. XPS is used to investigate CoPcF16 and CMK-3-CoPcF16 hybrid (**Fig. 1**). The fitting parameters of elements spectra for both materials are summarized in **Table 1**. As can be seen in both **Fig. 1** and **Table 1**, the C 1s spectrum of CoPcF16 is mainly composed by three main components (**Fig. 1 A and E**), which are attributed to the benzene C-C (C_β) (284.8 eV), pyrrolic C-N (C_α) (286.6 eV) and fluorinated carbon (C-F) (288.3 eV), respectively [28, 29]. In contrast, the C-F peak for CMK-3-CoPcF16 shifts to 289.2, which may be caused by the π-π interaction between CoPcF16 and CMK-3. An additional unknown peak at 283.3 was observed, which was often found in C on Co [30] or C-metal bond [31]. The unknown carbon peak might be caused by the influence of Co due to the strong π-π interaction. The Co spectra of both CMK-3-CoPcF16 and CoPcF16 show peaks for Co2p3/2 and Co2p1/2 with the binding energy of (781.5 eV, 796.8 eV) and (781.3 eV, 796.5 eV) respectively (**Fig. 1 D and H**), which are characteristic of Co (II) paramagnetic species, suggesting that CoPcF16 was successfully anchored into CMK-3 [32]. The peaks splits in the N1s (N_α and N_β) (**Fig. 2 B and F**) and F1s (F_γ) (**Fig. 2 C and G**) spectra of CMK-3-CoPcF16 were consistent with that of CoPcF16, indicating that the hybrid composite was successfully formed.

Fig 2. shows the Raman spectra of CMK-3-CoPcF16, CMK-3, and CoPcF16. Distinct D and G bands of CMK-3 are observed at 1315 and 1597 cm^{-1}, which is associated with the structural defects and E_{2g} vibration mode of sp2 carbon domains, respectively. After the immobilization of CoPcF16 molecules, D and G bands shift to 1306 and 1592 cm^{-1}, and the prominent peaks for pure CoPcF16 are also found in the spectra of the CMK-3-CoPcF16 composites. The decreased ID/IG ratio from 1.63 to 1.58 indicates the composites possess much larger average sp2 domain sizes and lower defect site densities. In addition, the low wavenumber shifts in D and G bands of CMK-3-CoPcF16 could be due to the π-π interaction between CMK-3 and CoPcF16 molecules [33],

The interaction between CMK-3 and CoPcF16 molecules is also investigated by EPR spectrum (**Fig. S-2, Supplemental information**). CMK-3 has a strong EPR response related to defects with a g factor value of 2.007. CoPcF16 presents a much higher EPR signal with g factor value of 2.584. The g-factor of CMK-3-CoPcF16 (2.258) is different from others, indicating that the electron dynamic is affected by the interaction between CMK-3 and attached CoPcF16 molecules [34].

The SEM and TEM images (**Fig. S-3 and Fig. S-4, Supplemental information**) of CMK-3-CoPcF16 hybrid show that CMK-3 remains its rod-like structure with an average diameter of about 500 nm and the length of 1 μm [35]. No aggregation of CoPcF16 was observed on the surface of CMK-3 (**Fig. S-4, Supplemental information**), suggesting that a highly molecular dispersion occurred due to the strong π-π interactions between CoPcF16 and CMK-3. In addition, energy dispersive

X-ray spectroscopy maps (**Fig. 3 and Fig. S-5, Supplemental information**) reveal that N, F and Co detected from CoPcF16 are homogeneously distributed over the CMK-3. The immobilization was also confirmed by electrochemical behaviors of CMK-3-CoPcF16/GCE (**Fig. 4**). The typical CV shows four pairs of well-defined redox peaks. A couple of redox peaks with formal potential of -0.85 V originates from the reversible process of $[Co(I)Pc(-2)F16]^{-}/[Co(I)Pc(-3)F16]^{2-}$ [36]. The second pair of redox peaks with formal potential of -0.31 V, is assigned to $[Co(II)Pc(-2)F16]/[Co(I)Pc(-2)F16]^{-}$ [37]. The other two pairs of shoulder peaks around -0.9 V and 0 V may be attributed to CoPcF16 anchored at different site of CMK-3. The fluorine substituent on the Pc ligand is another essential contributor, which further enhances the electrochemical performance. CoPc only shows excellent electrochemical behavior in organic solvent such as DMF and DMSO because of its limited solubility in water and inherent aggregation property [36]. The excellent electrochemical behavior of CMK-3-CoPcF16/GCE indicates that CoPcF16 is highly dispersed on CMK-3 without aggregation. The electron-withdrawing fluorine groups can also facilitate the formation of Co(I) [16], and consequently generate well defined electrochemical reaction between Co(II) and Co(I).

Electrochemical impedance spectroscopy (EIS) was performed for the electro-kinetic measurement of the electron-transfer reaction of the modified electrode (**Fig. S-6, Supplemental information).** A large semicircle domain is observed for CoPcF16/GCE, suggesting high charge transfer resistance since the electrode surface is covered by aggregated CoPcF16. Upon loading CoPcF16 on CMK-3, the resistance

significantly decreased, which is ascribed to high conductivity of supporting matrix and molecular state of CoPcF16.

3.2. Electrocatalytic oxidation towards H_2O_2 and sensing

The prepared CMK-3-CoPcF16 hybrid was then explored for the electrocatalytic oxidation towards H_2O_2. It is an important industrial and biological molecule, which plays an essential role as a signaling molecule in regulating many biological processes [38]. In addition, H_2O_2 has been widely used as an alternative liquid oxidant instead of gaseous oxygen in fuel cells especially used in air-free environments such as outer space and underwater [39]. **Fig. 5** shows the CVs of CMK-3/GCE (A), CoPcF16/GCE (B), and CoPcF16-CMK-3/GCE (C and D) in 0.1 M NaOH (dotted line) and 5 mM H_2O_2 (solid line) at a scan rate of 0.1 V/s, respectively. A reduction peak at -0.43 V occurs in H_2O_2 at CMK-3/GCE, but no obvious oxidation peak is observed though the anodic current increased along with potential (**Fig. 5 A**). This is attributed to the electrocatalytic activity of oxygen-containing species presented in CMK-3. In case of CoPcF16/GCE (**Fig. 5 B**), the reduction peak shifts to -0.3 V and two oxidation peaks are observed at about 0 V and 0.38 V, respectively. However, when the potential scans reversely (cathodic direction), the same oxidation wave as that at 0.38 V appears again. This suggests that CoPcF16 exhibited high electrocatalytic activity towards H_2O_2. The CoPcF16-CMK-3/GCE shows an couple of redox peaks with formal potential of -0.31 V ([Co(II)Pc(-2)F16]/[Co(I)Pc(-2)F16]$^-$) (**Fig. 5 C**) and presents multiple electrochemical processes for both the electro-oxidation and electro-reduction processes, companying with the lowest oxidation peak at -0.04 V

and the highest reduction peak potential at -0.23 V (**Fig. 5 D**), respectively. This result indicates that CoPcF16-CMK-3 demonstrate the highest electrocatalytic activity toward H_2O_2.

The electro-oxidation mechanism of H_2O_2 was further investigated by CVs at different scan rate **(Fig. 6).** The number of electrons involved in the overall H_2O_2 oxidation process (n) was calculated using the Randles–Sevcik equation for the irreversible electrode kinetics.

$$I_p = 2.99\times10^5\times A\times n\times[(1-\alpha)\times n_\alpha)]\times D^{1/2}\times C_0\times \upsilon^{1/2}$$

where, I_p, A, n, α, $n_{\alpha,}$ D, C_0, and υ are the peak current (A), electroactive surface area (cm^2), number of electron transfer, number of electron in rate determining step and electron transfer coefficient, diffusion coefficient (cm^2/s), concentration of (mol/ml), and scan rate (V/s). Considering the value of $(1-\alpha)\times n_\alpha$ (0.32) and diffusion coefficient (2×10^{-6} cm^2/s) [40], the number of electron transfer was found to be 2.1.

In order to explore the electrocatalytic processes of H_2O_2, oxygen reduction reaction (ORR) was also investigated the at CoPcF16-CMK-3 modified electrode. First, the CVs of CoPcF16-CMK-3/GCE in N_2- (dotted line) and O_2-saturated (solid line) 0.1 M NaOH solution were performed (**Fig. 7**). In O_2-saturated solution, distinct ORR response was observed, which is similar to the reduction curve in the presence of H_2O_2 (**Fig. 5 D**). Next, LSV was performed to assess the ORR kinetics and selectivity by using rotating (RRDE) in which ORR occurred at the disc electrode while the reduced product was oxidized at Pt ring electrode (**Fig. S-7, Supplemental information**). The disc voltammetric curve showed that ORR began at about -0.1 V,

and the reduction current increased with the negatively scanned potential until the limit diffusion current. The ring voltammetric curve also showed the same oxidation trend accompanying with ORR. The n is found to be in the range of 3.18-3.42 and the hydrogen peroxide yield (H_2O_2%) is in the range of 29-42% for CMK-3-CoPcF16 (**Fig. S-8, Supplemental information**), which is indicative of an incomplete reduction from O_2 to H_2O, that is, a mixed behavior between a 2- and 4-electron catalysis for the ORR. The electro-oxidation process of H_2O_2 was also investigated by RRDE in which electro-oxidation occurred at the disk electrode while the oxidized product was reduced at the Pt ring electrode (**Fig. S-9, Supplemental information**). It was found that the ring current occurred accompanying with the oxidation process of H_2O_2. The results showed that CoPcF16-CMK-3 composites exhibited high electrocatalytic activity for ORR. Therefore, we concluded that the electrochemical reaction of H_2O_2 is not a reversible process. The electro-oxidation of H_2O_2 to form O_2 is a two electrons process, but the reduction of product O_2 is a combined process (3.2 electrons) to form H_2O_2 and HO_2. Hence, the electro-oxidation mechanism of H_2O_2 can be speculated as follows.

CMK-3-[Co(I)Pc(-2)F16]$^-$ - e^- ⇄ CMK-3- Co(II)Pc(-2)F16]

CMK-3-[Co(II)Pc(-2)F16] + H_2O_2 + 2OH^- - e^-→ CMK-3-[Co(I)Pc(-2)F16]$^-$ + O_2 + 2H_2O

The effect of applied potential on the responses to H_2O_2 was studied. The optimal detection potential was found to be about 0 V (**Fig. S-10, Supplemental information.**). **Fig. 8** shows the amperometric response towards H_2O_2 at

CoPcF16-CMK-3/GCE. Upon addition of H_2O_2, the anodic current increases rapidly. The calibration plot shows that the increased current exhibits a linear relationship (R^2=0.9994) over a concentration range from 4.4 μM to 1.76 mM with a detection limit of 0.03 μM (S/N=3) and sensitivity of 132.7 $\mu A \bullet mM^{-1} \bullet cm^{-2}$. (**Fig. 8 A**). Sixteen repeated measurements of 20 μM H_2O_2 using the same electrode presents a relative standard deviation (RSD) value of 5.4% (**Fig. S-11, Supplemental information**). The stability of CoPcF16-CMK-3/GCE was further examined by a continuous performance. After 2000s of continuous operation for 5 μM H_2O_2, the electrode still retained 96% of its initial value (**Fig. S-12, Supplemental information**). The selectivity of the sensor was also investigated by exploring the response of interfering inorganic ions and biological species including glucose, ethanol, $NaNO_2$, NaCl, and $NaNO_3$ (**Fig. S-13, Supplemental information**). The results show that these common interfering species with 10-folds concentration did not interfere with the electrochemical detection of H_2O_2, indicating a high selectivity of the sensor. We also tested the interference from dopamine (DA), ascorbic acid (AA), and uric acid (UA) which are electrooxidizable constituents in physiological fluids (**Fig. S-14, Supplemental information**). It was found that the current value of DA, AA, and UA is 7.4 %, 30.1%, and 7.5%, respectively, relative to that of H_2O_2.

3.3. Electrocatalysis towards hydrazine oxidation and sensing

The CoPcF16-CMK-3/GCE was also found to be electroactive towards the oxidation of hydrazine. **Fig. 9** shows the CVs of CMK-3/GCE, CoPcF16/GCE, and CoPcF16-CMK-3/GCE of 5 mM hydrazine in a basic medium. CMK-3/GCE

demonstrates poor electrocatalytic activity towards hydrazine oxidation (**Fig. 9 A**). However, at CoPcF16/GCE, a well-defined oxidation peak is observed at about 0.12 V (**Fig. 9 B**). In case of CoPcF16-CMK-3/GCE (**Fig. 9 C**), the oxidation peak of hydrazine shifts to -0.07 V. The results indicate that CoPcF16-CMK-3/GCE shows excellent electrocatalytic activity due to highly dispersed CoPcF16 molecules on CMK-3.

The electron transfer number of hydrazine was further investigated by CV at different scan rate (**Fig. 10**). Assuming the value of $(1-\alpha)\times n_{\alpha}$ (0.45) and diffusion coefficient (2.0×10^{-6} cm^2/s) [41], the number of electron transfer was calculated to be 4.3 using the Randles–Sevcik equation for the irreversible electrochemical process of hydrazine. Hence, the mechanism was proposed as follows:

CMK-3-[Co(I)Pc(-2)F16]$^-$ - e^- ⇄ CMK-3--[Co(II)Pc(-2)F16]

CMK-3-[Co(II)Pc(-2)F16] + N_2H_4 + $4OH^-$ - $3e^-$ → CMK-3-[Co(I)Pc(-2)F16]$^-$ + N_2 + $4H_2O$

The effect of applied potential on the responses to hydrazine was studied and the optimal detection potential was found to be about 0 V (**Fig. S-15, Supplemental information**). The CoPcF16-CMK-3/GCE was next used for the amperometric sensing of hydrazine in a basic medium **(Fig. 11)**, and presented a linear response from 1 μM to 0.37 mM on the log-log plots (R^2=0.9992) with a detection limit of 0.2 μM (S/N=3) and sensitivity of 132.7 $\mu A \bullet mM^{-1} \bullet cm^{-2}$. Furthermore, for fifteen successive measurements of 5μM hydrazine, the RSD of response was found to be 5.7% (**Fig. S-16, Supplemental information**). The stability of

CoPcF16-CMK-3/GCE was further evaluated by a continuous test. After 2000s of continuous operation for hydrazine, the electrode still retained 91% of its initial value. The responses of CoPcF16-CMK-3/GCE to other species which are preferably found with hydrazine in real samples were also explored. We can see that no obvious responses are observed for 10-folds concentration of NaCl, KCl, Na_2SO_4, NaBr, $CaCl_2$, NaAc, glucose, $(NH_4)_2SO_4$, and $NaNO_3$ (**Fig. S-17, Supplemental information**). Hence, the fabricated electrochemical sensor is highly selective for hydrazine. The analytical performances for both H_2O_2 and hydrazine based on CoPcF16-CMK-3 and other bifunctional electrocatalysts reported in literature are summarized in **Table 2**. The CoPcF16-CMK-3 modified electrode exhibits low overpotential and detection limit, which are better than or compared to that based on other bifunctional electrocatalysts.

This sensor was also used to analyze the actual content of hydrazine in lake water. However, the calculated value did not accord with that obtained by spectrophotometry due to the interference of unknown complex species present in the sample. Potential application of CoPcF16-CMK-3/GCE was further explored for the detection of hydrazine spiked in lake water **(Fig. S-18, Supplemental information)**. The analytical results of hydrazine spiked in lake water were shown in the Supplemental information **(Table S-1)**.

4. Conclusions

We have demonstrated a simple, facile and fast method for non-covalently anchoring CoPcF16 molecules to CMK-3. CMK-3 was found to be a powerful

supporting platform for the immobilization of molecular CoPcF16. This is due to the stack effects of porous CMK-3 hybridization and fluorine substituents in the molecular structure, which endow the hybrid high electro-activity towards the oxidation of H_2O_2 and hydrazine. The molecular CoPcF16 immobilized in CMK-3 also exhibited high activity for ORR. An efficient electrochemical sensing platform was developed for sensitive detection of hydrogen peroxide and hydrazine. However, this sensor could not be used in situ analysis.

Acknowledgments

This work was funded by the Natural Science Foundation of Shandong Province (No.ZR2020MB058, ZR2020MB075). CF would like to express his gratitude to PALS for its support.

References

[1] Y. Wu, Z. Jiang, X. Lu, Y. Liang, H. Wang, Domino electroreduction of CO_2 to methanol on a molecular catalyst. Nature 575 (2019) 639-642.

[2] Z. Yue, C. Ou, N. Ding, L. Tao, J. Zhao, J. Chen,. Advances in metal phthalocyanine based carbon composites for electrocatalytic CO_2 reduction, ChemCatChem 12 (2020) 6103-6130.

[3] S. Dey, B. Mondal, S. Chatterjee, A. Rana, S.K. Amanullah, A. Dey, Molecular electrocatalysts for the oxygen reduction reaction, Nat. Rev. Chem. 1 (2017) 1-20.

[4] J.M. Gonçalves, B.A. Iglesias, P.R. Martins, L. Angnes, Recent advances in electroanalytical drug detection by porphyrin/phthalocyanine macrocycles: developments and future perspectives, Analyst 146 (2021) 365-381.

[5] A.R. Kottaichamy, S. Begum, M.C. Devendrachari, Z.M. Bhat, R. Thimmappa, H.M. Nimbegondi Kotresh, M.O. Thotiyl, Geometrical isomerism directed electrochemical sensing. Anal. Chem. 92 (2020) 4541-4547.

[6] P.C. Lo, M.S. Rodríguez-Morgade, R.K. Pandey, D.K. Ng, T. Torres, F. Dumoulin, The unique features and promises of phthalocyanines as advanced photosensitisers for photodynamic therapy of cancer, Chem. Soc. Rev. 49 (2020) 1041-1056.

[7] O.A. Melville, B.H. Lessard, T.P. Bender, Phthalocyanine-based organic

thin-film transistors: a review of recent advances, ACS Appl. Mater. Inter. 7(2015) 13105-13118.

[8] H. Peisert, J. Uihlein, F. Petraki, T. Chasse, Charge transfer between transition metal phthalocyanines and metal substrates: the role of the transition metal. J. Electron Spectrosc. Relat. Phenom. 204 (2015) 49-60.

[9] L. Lin, H. Li, C. Yan, H. Li, R. Si, M. Li, X. Bao, Synergistic catalysis over iron-nitrogen sites anchored with cobalt phthalocyanine for efficient CO_2 electroreduction. Adv. Mater. 31 (2019) 1903470.

[10] E. Boutin, M. Wang, J.C. Lin, M. Mesnage, D. Mendoza, B. Lassalle-Kaiser, M. Robert, Aqueous electrochemical reduction of carbon dioxide and carbon monoxide into methanol with cobalt phthalocyanine, Angew. Chem. Int. Edit. 58 (2019) 16172-16176.

[11] A.R. Kottaichamy, S. Begum, M.A. Nazrulla, N.C. Dargily, M. C. Devendrachari, Z. Manzoor Bhat, M.O. Thotiyl, Unprecedented isomerism–activity relation in molecular electrocatalysis. J. Phy. Chem. Let. 11 (2019) 263-271.

[12] S. Mukhopadhyay, A.R. Kottaichamy, Z.M. Bhat, N.C. Dargily, M.O. Thotiyl, Isomerism-activity relation in molecular electrocatalysis: a perspective, Electroanal. 32 (2020) 2387-2392.

[13] R. Li, X. Zhang, P. Zhu, D.K.P. Ng, N. Kobayashi, J. Jiang, Electron-donating or -withdrawing nature of substituents revealed by the electrochemistry of metal-free phthalocyanines, Inorg. Chem. 45 (2006) 2327-2334.

[14] D. Balle, H. Adler, P. Grüninger, R. Karstens, R. Ovsyannikov, E. Giangrisostomi, H. Peisert, Influence of the fluorination of Copc on the interfacial electronic structure of the coordinated metal ion, J. Phy. Chem. C 121 (2017) 18564-18574.

[15] M. Wang, K. Torbensen, D. Salvatore, S. Ren, D. Joulié, F. Dumoulin, M. Robert, CO_2 electrochemical catalytic reduction with a highly active cobalt phthalocyanine, Nat. Commun. 10 (2019) 1-8.

[16] X. Zhang, Z. Wu, X. Zhang, L. Li, Y. Li, H. Xu, H. Wang, Highly selective and active CO_2 reduction electrocatalysts based on cobalt phthalocyanine/carbon nanotube hybrid structures, Nat. Commun. 8 (2017) 1-8.

[17] J. Wang, X. Huang, S. Xi, J.M. Lee, C. Wang, Y. Du, X. Wang, Linkage effect in the heterogenization of cobalt complexes by doped graphene for electrocatalytic CO_2 reduction, Angew. Chem. Int. Edit. 58 (2019) 13532-13539.

[18] T. Honda, T. Kojima, S. Fukuzumi, Proton-coupled electron-transfer reduction of dioxygen catalyzed by a saddle-distorted cobalt phthalocyanine, J. Am. Chem. Soc. 134 (2012) 4196-4206.

[19] J. Choi, P. Wagner, S. Gambhir, R. Jalili, D.R. MacFarlane, G.G. Wallace, D.L. Officer, Steric modification of a cobalt phthalocyanine/graphene catalyst to give enhanced and stable electrochemical CO2 reduction to CO, ACS Energy Lett. 4 (2019) 666-672.

[20] N. Han, Y. Wang, L. Ma, J. Wen, J. Li, H. Zheng, Y. Li, Supported cobalt polyphthalocyanine for high-performance electrocatalytic CO2

reduction, Chem 3 (2017) 652-664.

[21] P. Li, Y. Ding, A. Wang, L. Zhou, S. Wei, Y. Zhou, T. Lu, Self-assembly of tetrakis (3-trifluoromethylphenoxy) phthalocyaninato cobalt (II) on multiwalled carbon nanotubes and their amperometric sensing application for nitrite, ACS Appl. Mater. Inter. 5 (2013) 2255-2260.

[22] M.R. Benzigar, S.N. Talapaneni, S. Joseph, K. Ramadass, G. Singh, J. Scaranto, A. Vinu, Recent advances in functionalized micro and mesoporous carbon materials: synthesis and applications, Chem. Soc. Rev. 47 (2018) 2680-2721.

[23] R. Ryoo, S.H. Joo, S. Jun, Synthesis of highly ordered carbon molecular sieves via template-mediated structural transformation, J. Phy. Chem. B 103 (1999) 7743-7746.

[24] A. Walcarius, Electrocatalysis, sensors and biosensors in analytical chemistry based on ordered mesoporous and macroporous carbon-modified electrodes. TrAC Trend Anal. Chem. 38 (2012), 79-97.

[25] J.C. Ndamanisha, L.P. Guo, Ordered mesoporous carbon for electrochemical sensing: a review. Analytica chimica acta, 747 (2012) 19-28.

[26] A. Walcarius, Recent trends on electrochemical sensors based on ordered mesoporous carbon. Sensors, 17 (2017) 1863.

[27] N. Pereira-Rodrigues, R. Cofré, J.H. Zagal, F. Bedioui, Electrocatalytic activity of cobalt phthalocyanine CoPc adsorbed on a graphite electrode for the oxidation of reduced l-glutathione (GSH) and the reduction of its disulfide (GSSG) at physiological pH, Bioelectrochem. 70 (2007) 147-154.

[28] M. Toader, P. Shukrynau, M. Knupfer, D.R. Zahn, M. Hietschold, Site-dependent donation/backdonation charge transfer at the CoPc/Ag (111) interface, Langmuir 28 (2012) 13325-13330.

[29] A. Tressaud, F. Moguet, S. Flandrois, M. Chambon, C. Guimon, G. Nanse, O.P. Bahl, On the nature of C-F bonds in various fluorinated carbon materials: XPS and TEM investigations, J. Phy. Chem. Solids 57 (1996) 745-751.

[30] C.J. Weststrate, A.C. Kızılkaya, E.T. Rossen, M.W. Verhoeven, I.M. Ciobîcă, A.M. Saib, J.W. Niemantsverdriet, Atomic and polymeric carbon on Co (0001): surface reconstruction, graphene formation, and catalyst poisoning, J. Phy. Chem. C 116 (2012) 11575-11583.

[31] Y. Li, L. Zhu, T. Yao, T. Liu, R. Qian, F. Li, H. Wang, Space-confined synthesis of ultrasmall SnO_2 nanodots within ordered mesoporous carbon CMK-3 for high-performance lithium ion batteries, Energ. Fuel. 34 (2020) 7709-7715.

[32] D.K. Singh, V. Ganesan, D.K. Yadav, M. Yadav, Metal (Mn, Fe, Co, Ni, Cu, and Zn) phthalocyanine-immobilized mesoporous carbon nitride materials as durable electrode modifiers for the oxygen reduction reaction, Langmuir 36 (2020) 12202-12212.

[33] M. Li, X. Bo, Y. Zhang, C. Han, L. Guo, Comparative study on the oxygen reduction reaction electrocatalytic activities of iron phthalocyanines supported on reduced graphene oxide, mesoporous carbon vesicle, and ordered mesoporous carbon. Journal of Power Sources, 264 (2014), 114-122.

[34] J. Riquelme, K. Neira, J.F. Marco, P. Hermosilla-Ibáñez, W. Orellana, J.H. Zagal,

F. Tasca, Biomimicking vitamin B12. A Co phthalocyanine pyridine axial ligand coordinated catalyst for the oxygen reduction reaction, Electrochim. Acta, 265 (2018) 547-555.

[35] B. Yuan, H. Wang, J. Cai, Y. Peng, Y. Niu, H. Chen, C. Xu, A novel oxidation-reduction method for highly selective detection of cysteine over reduced glutathione based on synergistic effect of fully fluorinated cobalt phthalocyanine and ordered mesoporous carbon. Sens. Actuators B: Chem. 288 (2019) 180-187.

[36] B.R. Kozub, R.G. Compton, Voltammetric studies of the redox mediator, cobalt phthalocyanine, with regard to its claimed electrocatalytic properties, Sens. Actuators B: Chem. 147 (2010) 350-358.

[37] N. Pereira-Rodrigues, R. Cofré, J.H. Zagal, F. Bedioui, Electrocatalytic activity of cobalt phthalocyanine CoPc adsorbed on a graphite electrode for the oxidation of reduced l-glutathione (GSH) and the reduction of its disulfide (GSSG) at physiological pH, Bioelectrochem. 70 (2007) 147-154.

[38] R. Zhang, W. Chen, Recent advances in graphene-based nanomaterials for fabricating electrochemical hydrogen peroxide sensors, Biosens. Bioelectron. 89 (2017) 249-268.

[39] L. An, T. Zhao, X. Yan, X. Zhou, P. Tan, The dual role of hydrogen peroxide in fuel cells, Sci. Bull. 60 (2015) 55-64.

[40] A. Arjunan, A. Sukeri, D.P.M. Saraiva, P.B. Miranda, M. Bertotti, Electrochemical Studies of Hydrogen Peroxide Oxidation on a Nanoporous Gold

Surface: Fundamental and Analytical Applications. J. Electrochem.l Soc. 16 (2020) 116507.

[41] S.M. Golabi, H.R. Zare, Electrocatalytic oxidation of hydrazine at a chlorogenic acid (CGA) modified glassy carbon electrode. J. electroanal. Chem. 465 (1999), 168-176.

[42] B. Yuan, P. Sun, L. Zhao, D. Zhang, Y. Zhang, C. Qi, C. Xu, Pd nanoparticles supported on 1, 10-phenanthroline-5, 6-dione modified graphene oxide as superior bifunctional electrocatalyst for highly sensitive sensing, J. Electroanal. Chem. 861 (2020) 113945.

[43] A. Othmani, Z. Kouki, S. Kouass, F. Touati, H. Dhaouadi, A highly sensitive hydrazine and hydrogen peroxide non-enzymatic sensor based on CuO nanoplatelets, J. Mater. Sci. Mater. El. (2020) 1-11.

[44] N.M. Umesh, K. Kohilarani, R. Devasenathipathy, B. Sriram, Y.X. Liu, S.F. Wang, Preparation of Co-MOF derived $Co(OH)_2$/multiwalled carbon nanotubes as an efficient bifunctional electro catalyst for hydrazine and hydrogen peroxide detections, J. Taiwan Inst. Chem. E. 93 (2018) 79-86.

[45] P. Mayuri, S.T. Huang, V. Manic, A.S. Kumar, A new organic redox species-indole tetraone trapped MWCNT modified electrode prepared by in-situ electrochemical oxidation of indole for a bifunctional electrocatalysis and simultaneous flow injection electroanalysis of hydrazine and hydrogen peroxide, Electrochim. Acta 268 (2018) 150-162.

[46] A.A. Ensafi, M.M. Abarghoui, B. Rezaei, Facile synthesis of Pt-Cu@silicon

nanostructure as a new electrocatalyst supported matrix, electrochemical detection of hydrazine and hydrogen peroxide, Electrochim. Acta 190 (2016) 199-207.

[47] S. Majumder, B. Saha, S. Dey, R. Mondal, S. Kumar, S. Banerjee, A high sensitive non-enzymatic hydrogen peroxide and hydrazine electrochemical sensor based on 3D micro-snowflakes architectures of α-Fe_2O_3, RSC Adv. 6 (2016) 59907-59918.

[48] C. Li, M. Li, X.J. Bo, L. Yang, A.C. Mtukula, L.P. Guo, Facile synthesis of electrospinning Mn_2O_3-Fe_2O_3 loaded carbon fibers for electrocatalysis of hydrogen peroxide reduction and hydrazine oxidation, Electrochim. Acta 211 (2016) 255-264.

[49] Y.J. Yang, W.K. Li, X.M. Wu, Copper sulfide| reduced graphene oxide nanocomposite for detection of hydrazine and hydrogen peroxide at low potential in neutral medium, Electrochim. Acta 123 (2014) 260-267.

[50] K.K. Lee, P.Y. Loh, C.H. Sow, W.S. Chin, CoOOH nanosheet electrodes: Simple fabrication for sensitive electrochemical sensing of hydrogen peroxide and hydrazine, Biosens. Bioelectron. 39 (2013) 255-260.

[51] M. Rajkumar, C.P. Hong, S.M. Chen, Electrochemical synthesis of palladium nano urchins decorated multi walled carbon nanotubes for electrocatalytic oxidation of hydrazine and reduction of hydrogen peroxide, Int. J. Electrochem. Sci. 8 (2013) 5262-5274.

[52] B. Šljukic, C.E. Banks, A. Crossley, R.G. Compton, Iron (III) oxide graphite

composite electrodes: application to the electroanalytical detection of hydrazine and hydrogen peroxide, Electroanal. 18 (2006) 1757-1762.

[53] Y.H. Wang, X.J. Yang, J. Bai, X. Jiang, G.Y. Fan, High sensitivity hydrogen peroxide and hydrazine sensor based on silver nanocubes with rich {100} facets as an enhanced electrochemical sensing platform, Biosens. Bioelectron. 43 (2013) 180-185.

[54] J.P. Metters, F. Tan, R.O. Kadara, C.E. Banks, Platinum screen printed electrodes for the electroanalytical sensing of hydrazine and hydrogen peroxide, Anal. Methods 4 (2012) 1272-1277.

Figure Captions

Fig. 1 XPS narrow scan of the C1s (A, E), N1s (B, F), F 1s (C, G), Co 2p (D, H) region for CoPcF16-CMK-3 (A, B, C, and D) and CoPcF16 (E, F, G, and H).

Fig. 2 Raman spectra of CMK-3-CoPcF16, CMK-3 and CoPcF16.

Fig. 3 A typical TEM image (a) of CMK-3-CoPcF16 for elemental distribution and the elemental mapping of carbon (b), nitrogen (c), oxygen (d), fluorine (e), and Cobalt (f).

Fig. 4 CV of CoPcF16-CMK-3/GCE in 0.1 M PBS (pH 7.0) at a scan rate of 0.1 V/s.

Fig. 5 CVs of CMK-3/GCE (A), CoPcF16/GCE (B), and CoPcF16-CMK-3/GCE (C and D) in 0.1 M NaOH solution in the absence (dotted line) and presence (solid line) of 5 mM H_2O_2 at a scan rate of 0.1 V/s.

Fig. 6 CVs of CoPcF16-CMK-3/GCE in 0.1 M NaOH solution in the presence of H_2O_2 at different scan rate. Inset: calibration plot for the current versus the square root of scan rate.

Fig. 7 CVs of CMK-3-CoPcF16/GCE in N_2- (dotted line) and O_2-saturated (solid line) 0.1 M NaOH solution at 25mV/s.

Fig. 8 Amperometric response of CoPcF16-CMK-3/GCE to the successive addition of H_2O_2 in stirred 0.1 M NaOH solution at an applied potential of 0 V. *Inset* (A) is the

calibration plot for the steady-state current versus H_2O_2 concentrations. *Inset* (B) is the amperometric response at low H_2O_2 concentration.

Fig. 9 CVs of CMK-3/GCE (A), CoPcF16/GCE (B), and CoPcF16-CMK-3/GCE (C) in 0.1 M NaOH solution in the absence (dotted line) and presence (solid line) of 5 mM hydrazine at a scan rate of 0.1 V/s.

Fig. 10 CVs of CoPcF16-CMK-3/GCE in 0.1 M NaOH solution in the presence of hydrazine at different scan rate. Inset: calibration plot for the current versus the square root of scan rate.

Fig. 11 Amperometric response of CoPcF16-CMK-3/GCE to the successive addition of hydrazine in stirred 0.1 M NaOH solution at an applied potential of 0 V. *Inset* (A) is the log-log calibration plot for the steady-state current versus hydrazine concentrations. *Inset* (B) is the amperometric response at low hydrazine concentration.

Fig. 1

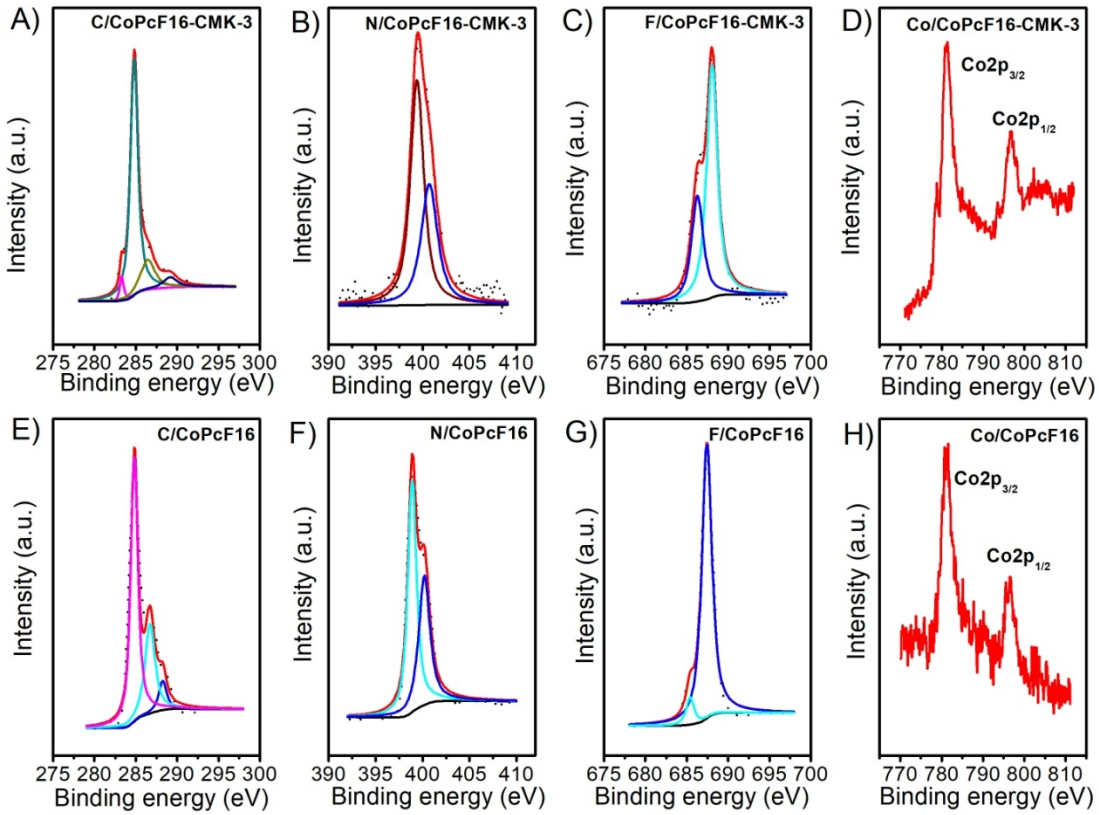
A)
C/CoPcF16-CMK-3
B)
N/CoPcF16-CMK-3
C)
F/CoPcF16-CMK-3
D)
Co/CoPcF16-CMK-3
Co2p3/2
Co2p1/2
E)
C/CoPcF16
F)
N/CoPcF16
G)
F/CoPcF16
H)
Co/CoPcF16
Co2p3/2
Co2p1/2
Intensity (a.u.)
Binding energy (eV)
275 280 285 290 295 300
390 395 400 405 410
675 680 685 690 695 700
770 780 790 800 810

Fig. 2

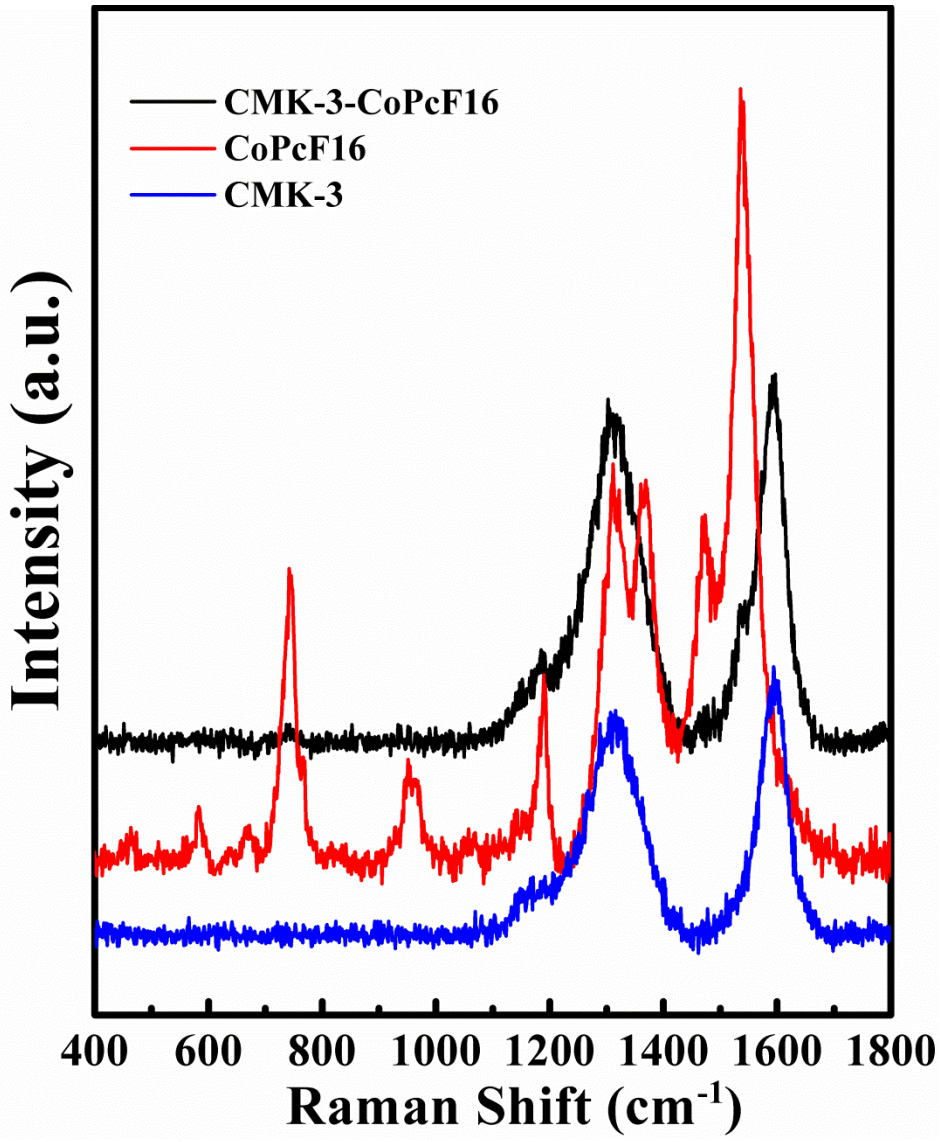
CMK-3-CoPcF16
CoPcF16
CMK-3
Intensity (a.u.)
400
600
800
1000
1200
1400
1600
1800
Raman Shift (cm-1)

Fig. 3

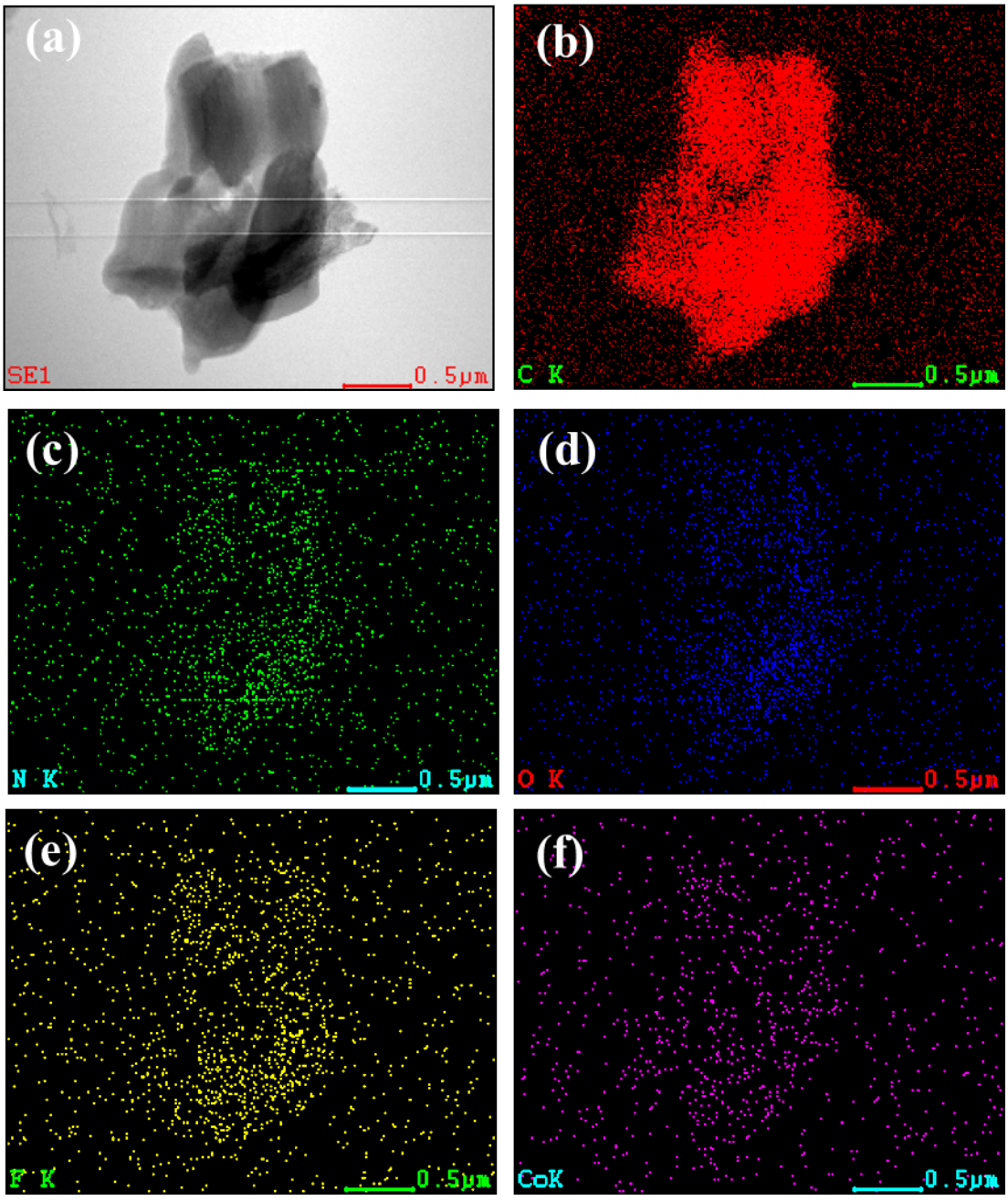

Fig. 4

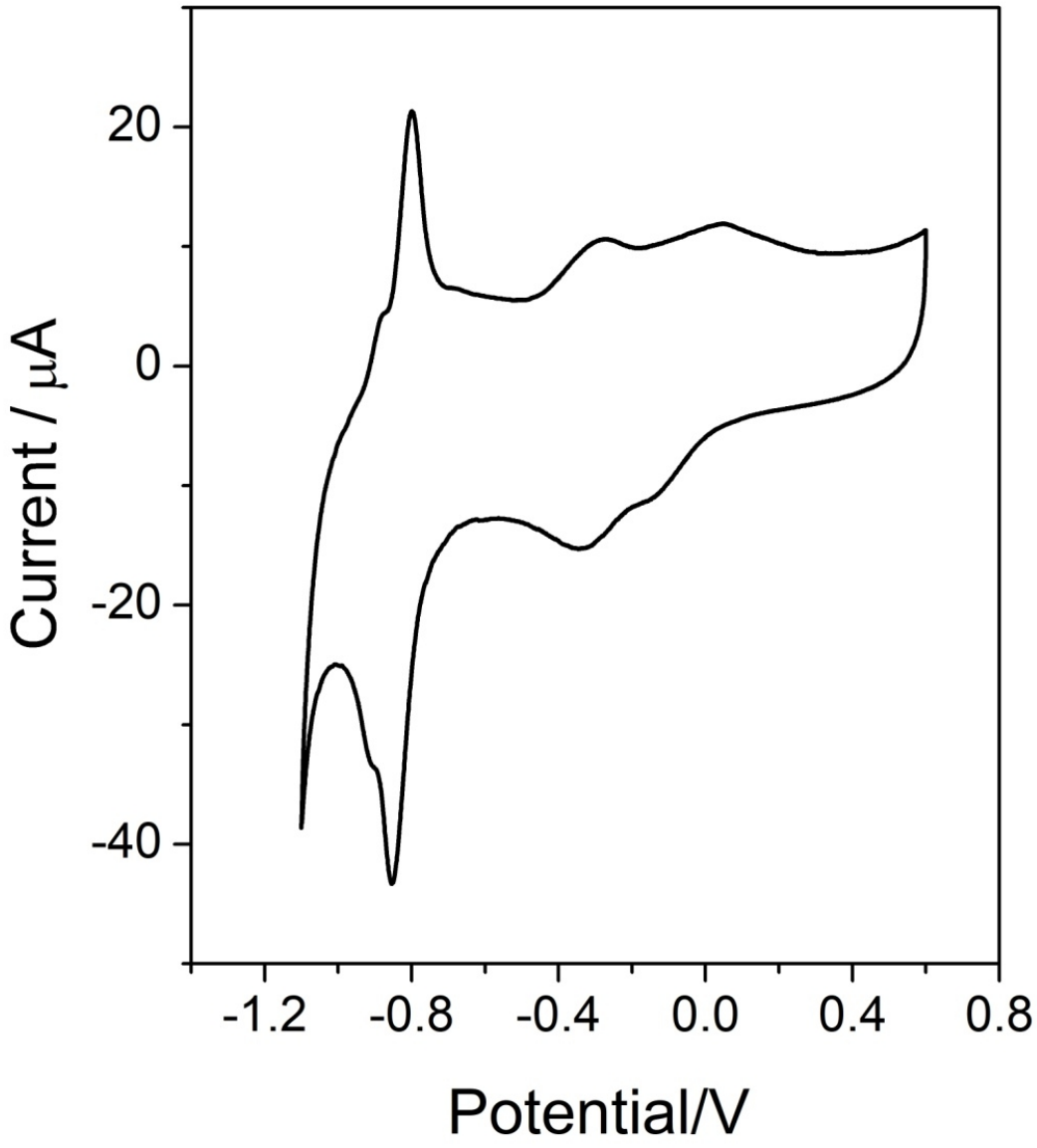

Fig. 5

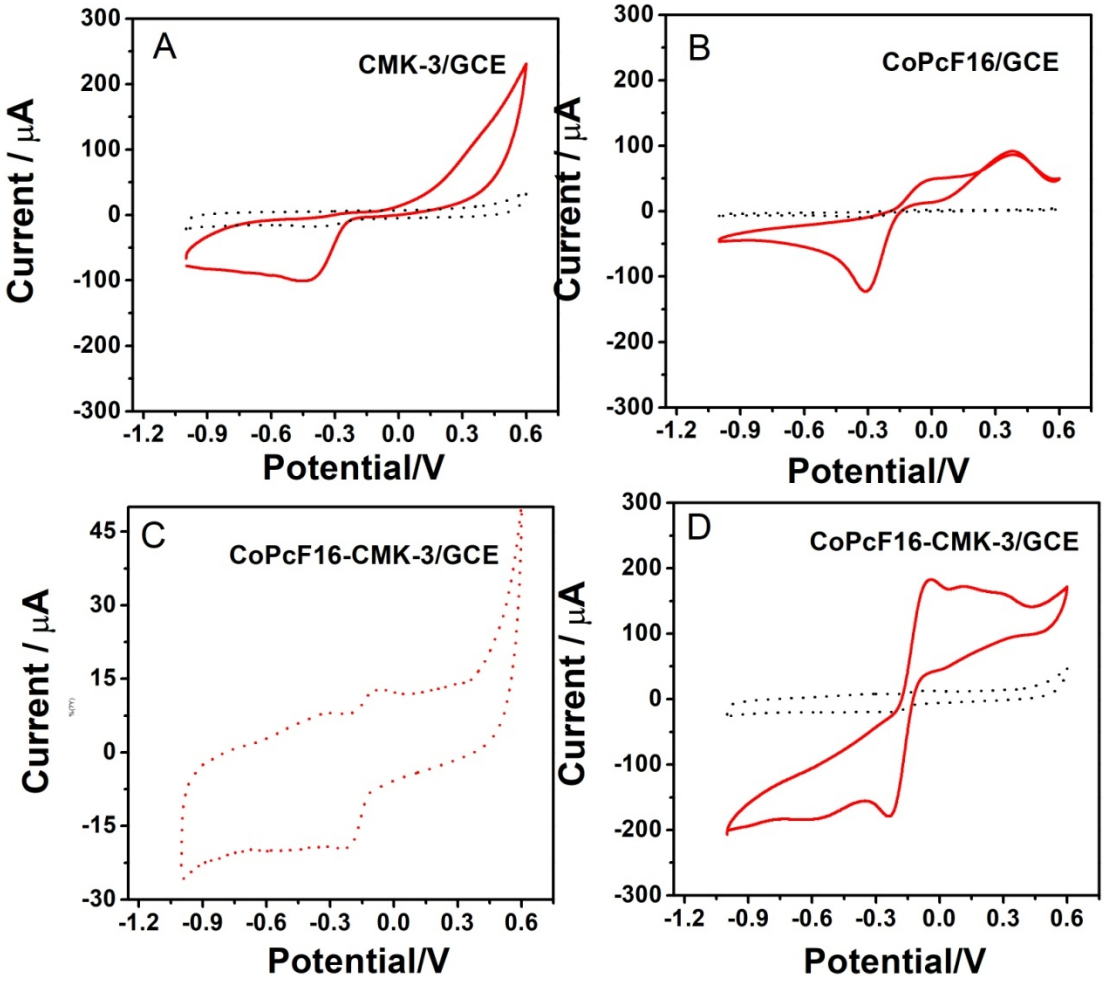
A
CMK-3/GCE
B
CoPcF16/GCE
C
CoPcF16-CMK-3/GCE
D
CoPcF16-CMK-3/GCE
Current / μA
Potential/V

Fig. 6

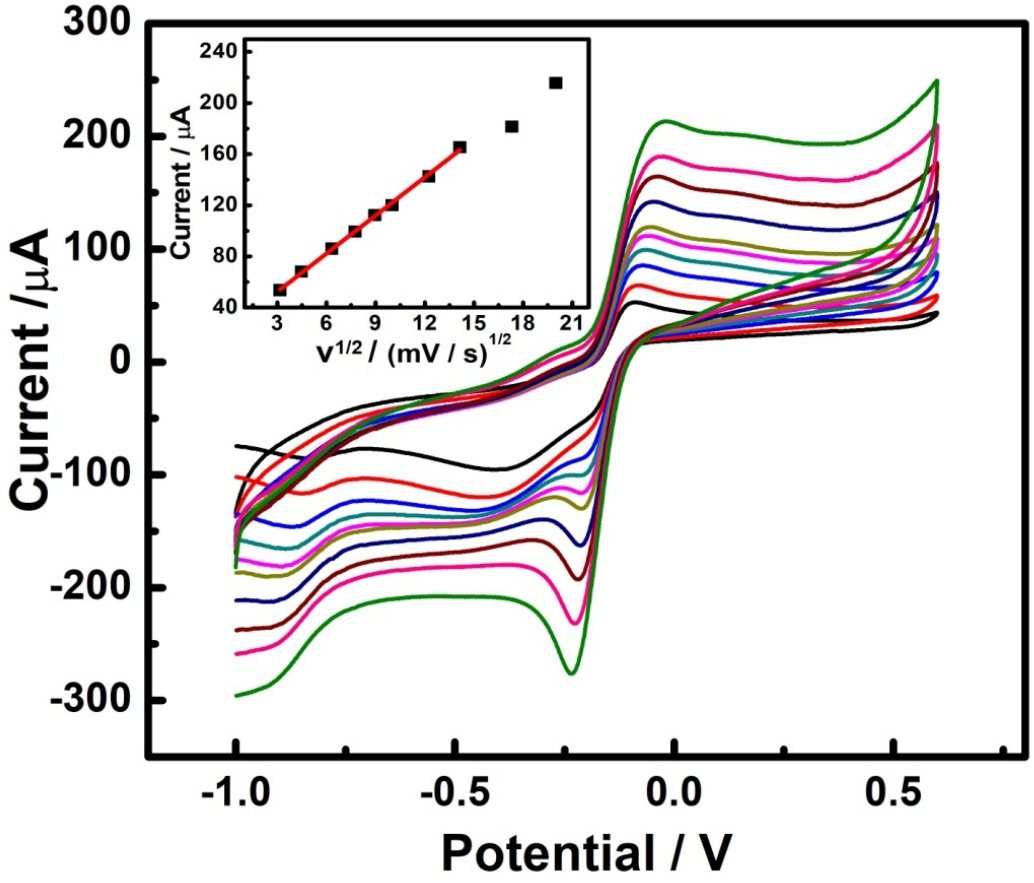
Current /μA
Potential / V
300
200
100
0
-100
-200
-300
-1.0
-0.5
0.0
0.5
Current / μA
240
200
160
120
80
40
3
6
9
12
15
18
21
v^1/2 / (mV / s)^1/2

Fig. 7

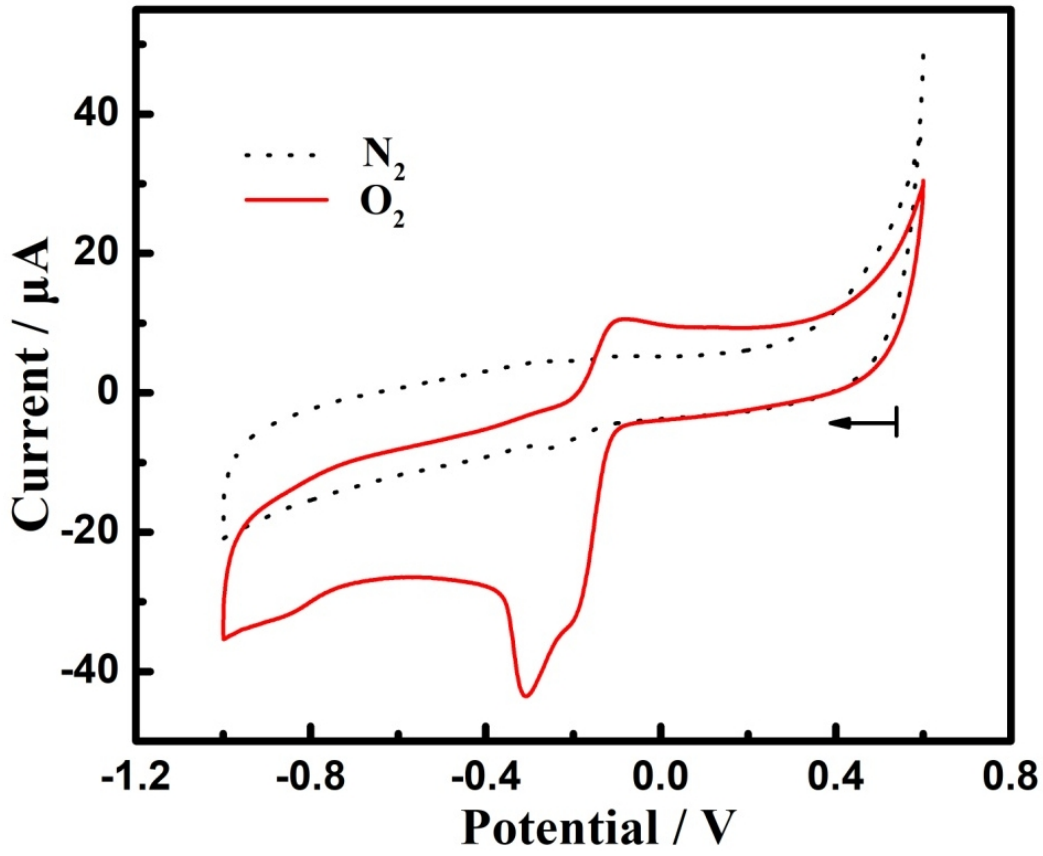

Fig. 8

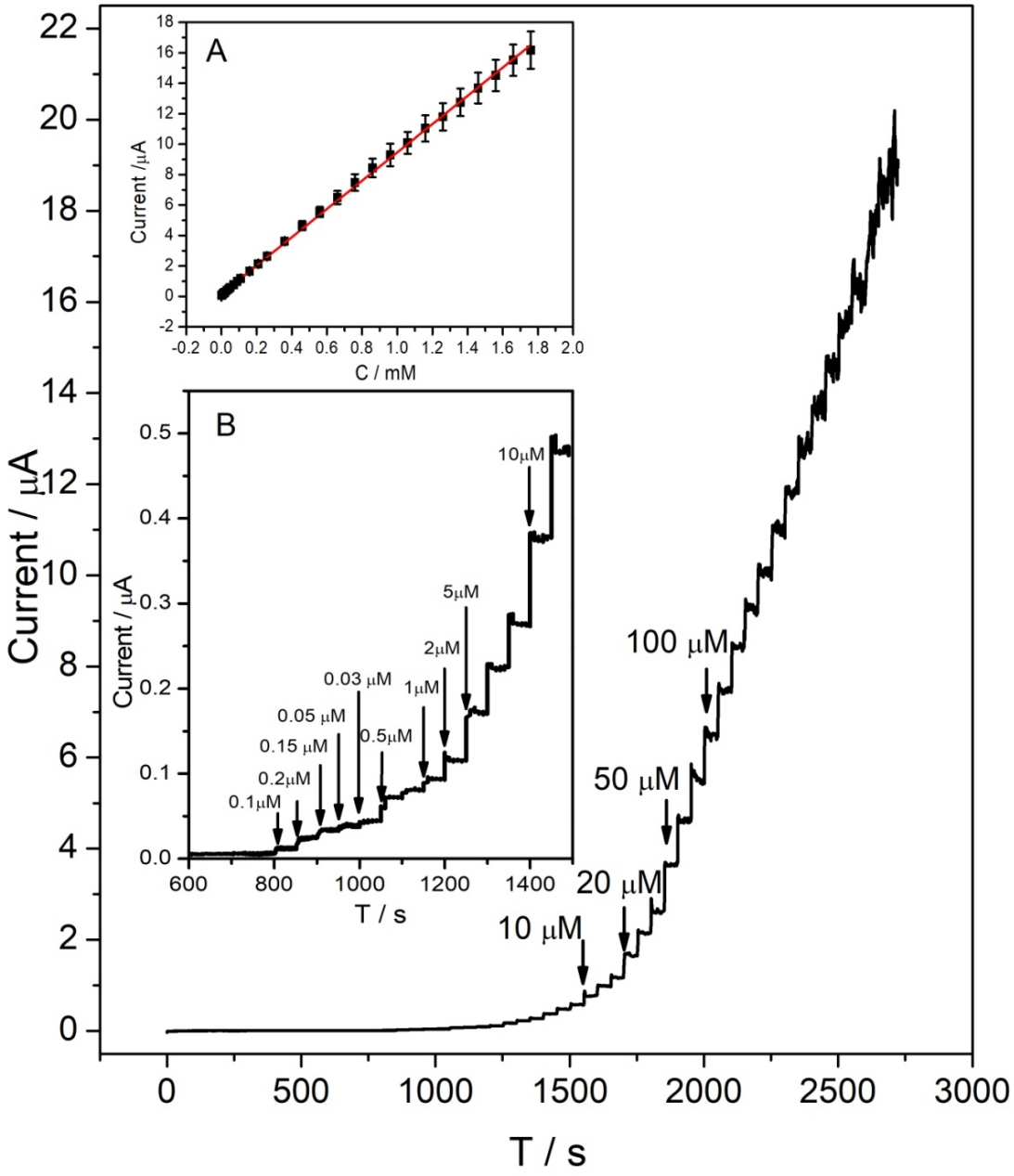
A
Current /μA
C / mM
B
Current / μA
T / s
0.1μM
0.2μM
0.15 μM
0.05 μM
0.03 μM
0.5μM
1μM
2μM
5μM
10μM
10 μM
20 μM
50 μM
100 μM
Current / μA
T / s

Fig. 9

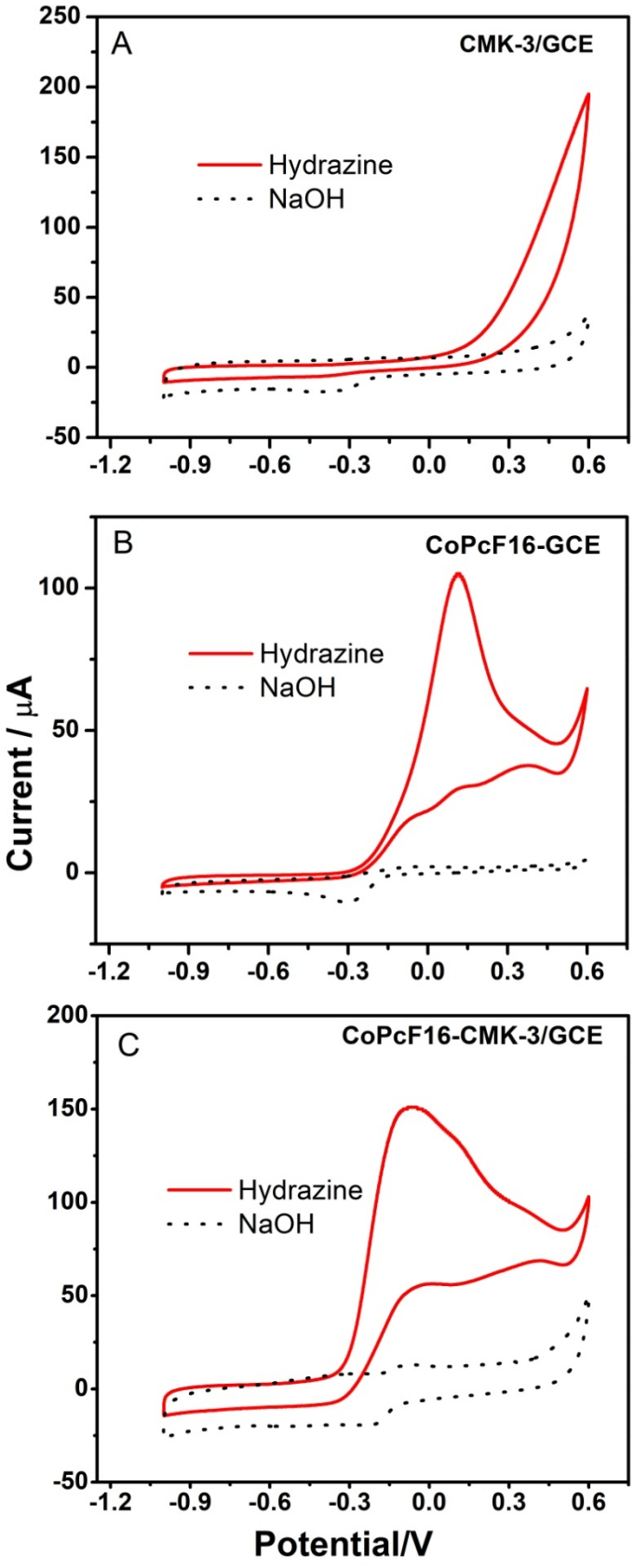
A
CMK-3/GCE
Hydrazine
NaOH
B
CoPcF16-GCE
Hydrazine
NaOH
C
CoPcF16-CMK-3/GCE
Hydrazine
NaOH
Current / μA
Potential/V

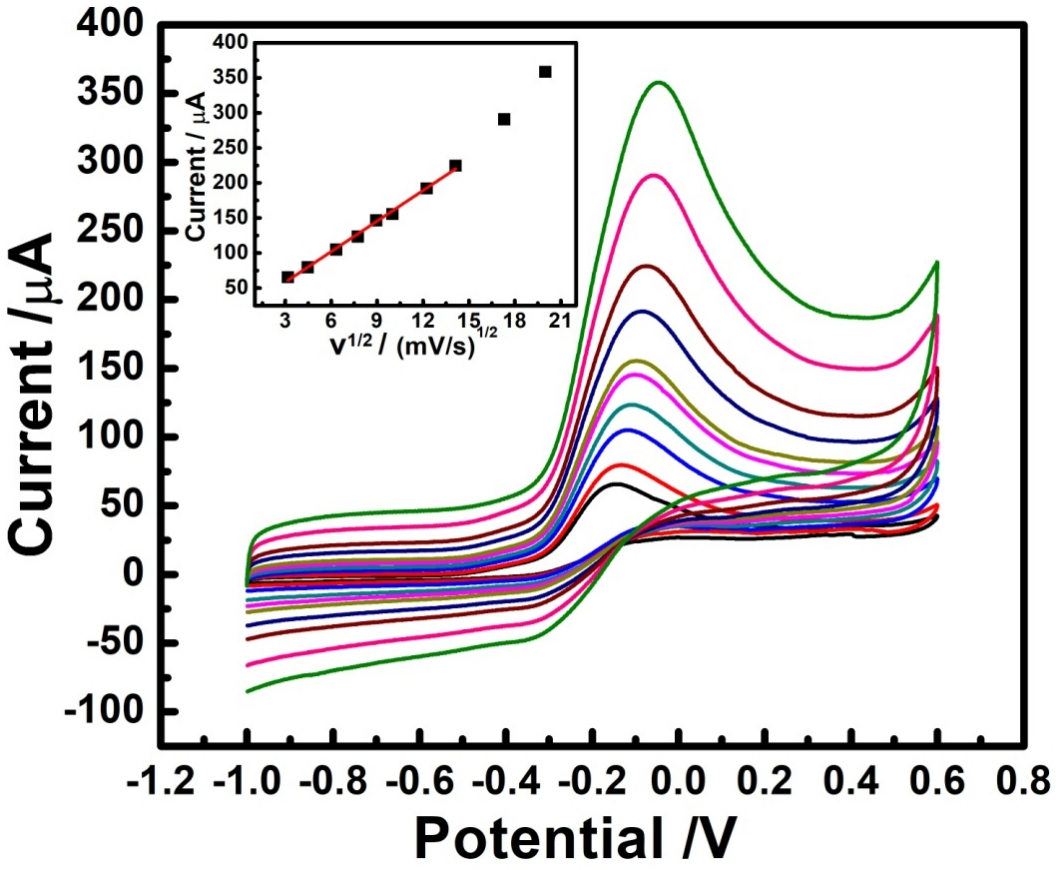
Current /μA
Potential /V
400
350
300
250
200
150
100
50
0
-50
-100
-1.2 -1.0 -0.8 -0.6 -0.4 -0.2 0.0 0.2 0.4 0.6 0.8
Current / μA
400
350
300
250
200
150
100
50
3 6 9 12 15 18 21
V^1/2 / (mV/s)^1/2

Fig. 10

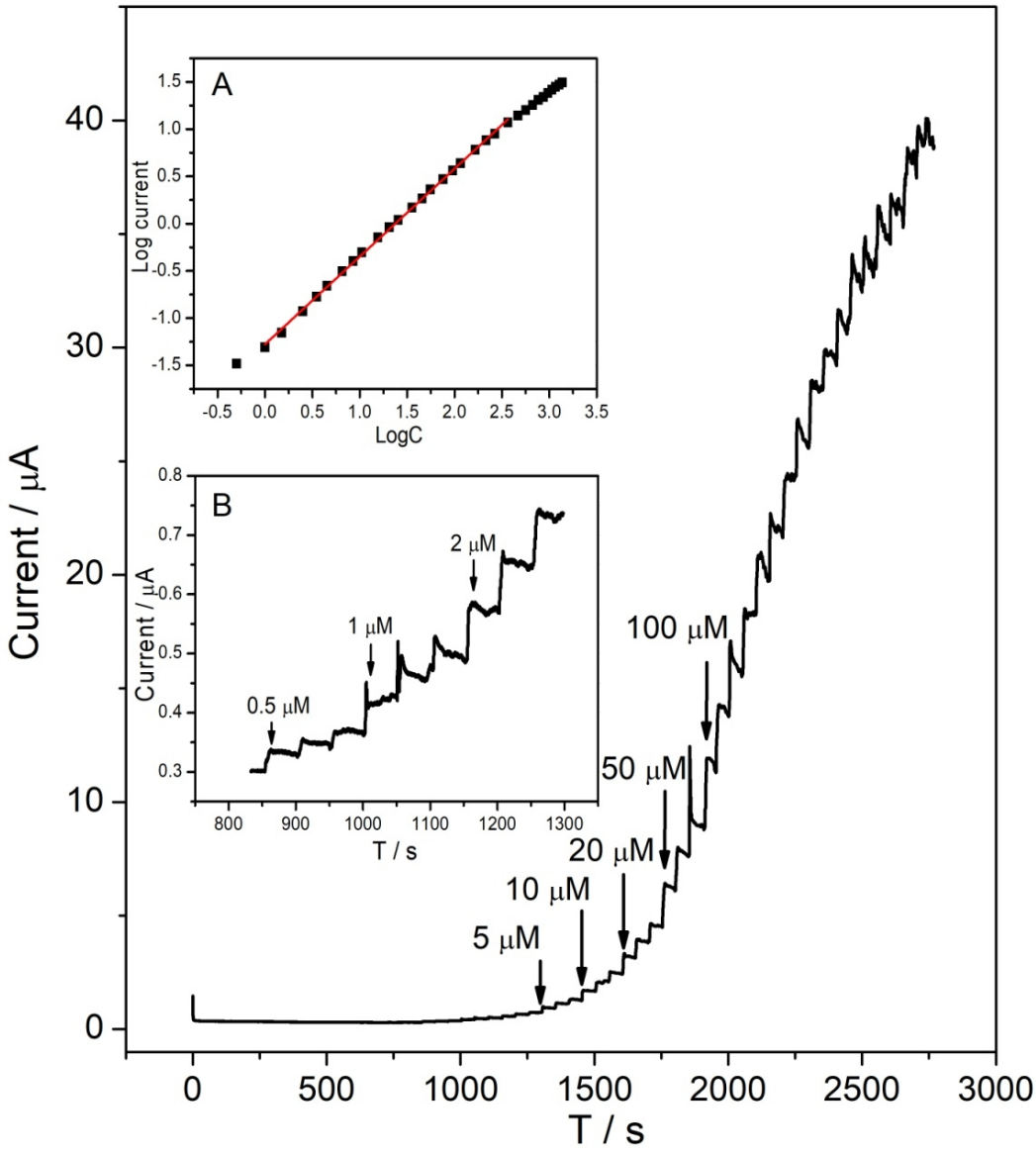
A
Log current
LogC
B
Current / μA
T / s
0.5 μM
1 μM
2 μM
5 μM
10 μM
20 μM
50 μM
100 μM
Current / μA
T / s

Fig. 11

Material	Binding energy									
	C				Co		N		F	
	C-C (C_β)	C-N (C_α)	C-F (C_γ and C_δ)	Unknown peak	$Co2p_{3/2}$	$Co2p_{1/2}$	Co-N-C (N_α)	N-C (N_β)	F_γ	F_δ
CMK-3-CoPcF16	284.8	286.5	289.2	283.3	781.5	796.8	399.4	400.7	686.3	688.0
CoPcF16	284.8	286.7	288.3		781.3	796.5	398.9	400.2	685.4	687.4

Table 1. Binding energy for different elements of CMK-3-CoPcF16 and CoPcF16

Table 2. Electrochemical sensing performances for H_2O_2 and hydrazine based on CoPcF16-CMK-3 and other bifunctional electrocatalysts.

Materials	H_2O_2				Hydrazine				Ref
	pH	Peak potential (V)[c]	Linear range (μM)	LOD (μM)	pH	Potential (V)[c]	Linear range (μM)	LOD (μM)	
Pd-phen-dione/ER-GO	7.2	-0.3 [a]	0.5-1079	0.07	7.2	0.3	0.1-1166	0.04	[42]
CuO nanoplatelets	13	0.55 [b]	1-1800	0.3	13	0.55	1-1200	0.1	[43]
MWCNTs-$Co(OH)_2$	13	-0.2[a]	5-550	1.36	13	0.1	0.2-1106	0.084	[44]
MWCNTs@Indole-tetraone	7.0	-0.25[a]	250-3500		7.0	0.25	500-4000		[45]
Pt-Cu/Si	7.0	-0.25[a]	0.5-1280	0.1	13	0.2	0.2-1680	0.05	[46]
Fe_2O_3	13	-0.8[a]	100-5500	10	13	0.1	50-1340	5	[47]
Mn_2O_3-Fe_2O_3	13	-0.4 [a]	10-15400	0.60	7.0	0.7	0.5-1200	0.09	[48]
CuS/rGO	7.0	-0.2[a]	1-1000	0.1	7.0	0.4	1-1000	0.3	[49]
CoOOH	13	0.1[b]	0-1600	40	13	0.1	0-1000	20	[50]
Pd/MWCNTs	1	-0.088[a]	1-19	0.1	1	0.277	0-100	1	[51]
Fe_2O_3/graphite	7.4	-0.6[a]	200-5500	3.5	7.4	0.7	-10	1.2	[52]
PVP/Ag	6.5	-0.47[a]	50-70000	0.18	7.4	0.28	5-460	1.1	[53]
Pt	7.0	0.35[a]	100-1000	0.14	7.0	0.7	50-500	0.15	[54]
CoPcF16-CMK-3	13	-0.23 [a] -0.04 [b]	4.4-1760	0.03	13	-0.07	1-370	0.2	This work

[a]: Reduction potential; [b]: Oxidation potential; [c]: versus Ag/AgCl;

Supplementary information

Molecular fluorinated cobalt phthalocyanine immobilized on ordered mesoporous carbon as an electrochemical sensing platform for sensitive detection of hydrogen peroxide and hydrazine in alkaline medium

Baiqing Yuan [a, *], Peng Sun [a], Carlos Fernandez [b, *], Hemin Wang [a], Peiyu Guan [a], Hui Xu [c], Yuzhong Niu [a, *]

[a] School of Chemistry and Materials Science, Ludong University, Yantai 264025, Shandong, China

[b] School of Pharmacy and Life Sciences, Robert Gordon University, Garthdee Road, Aberdeen AB10 7GJ, United Kingdom

[c] College of Science and Engineering, Huzhou College, Huzhou 313000, China

*** Corresponding author.**

E-mail: baiqingyuan1981@126.com (B. Yuan); c.fernandez@rgu.ac.uk (C.Fernandez); niuyuzhong@ldu.edu.cn (Y, Niu)

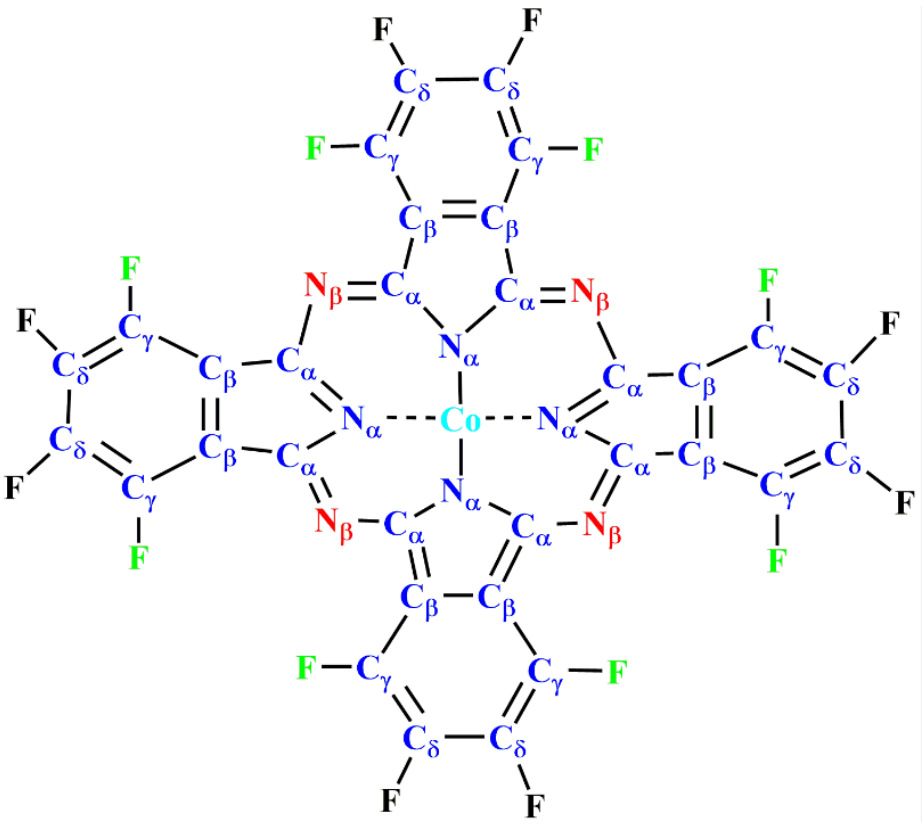

Fig. S-1 Molecular structure of CoPcF16.

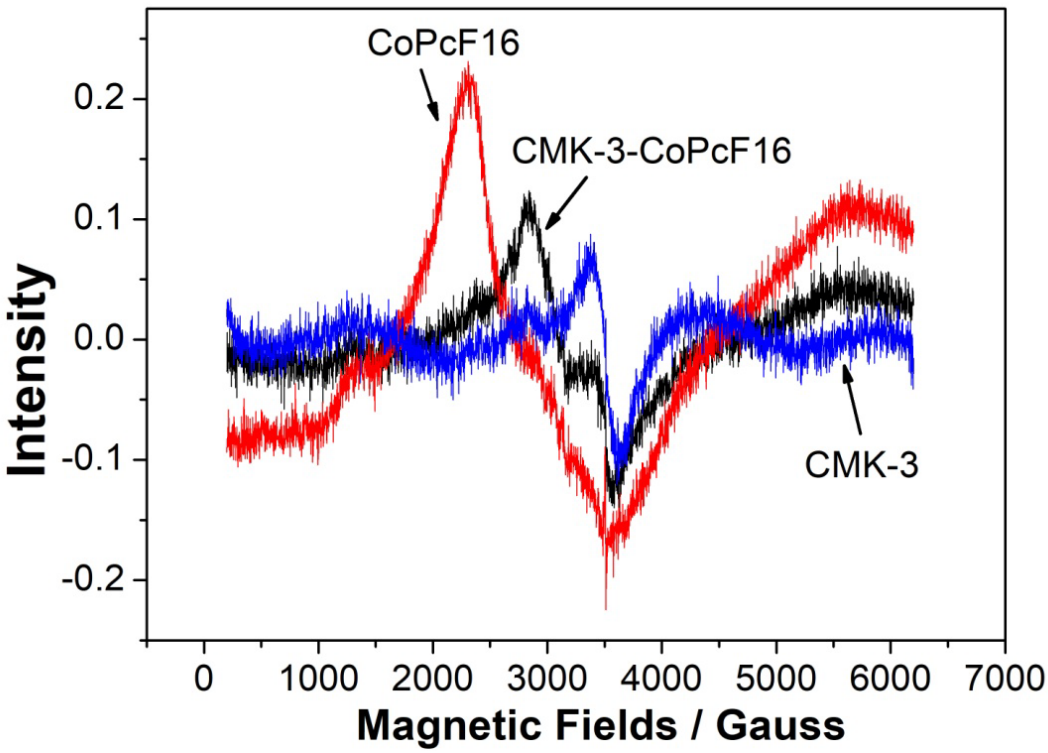

Fig. S-2 EPR spectra of CMK-3-CoPcF16, CMK-3 and CoPcF16

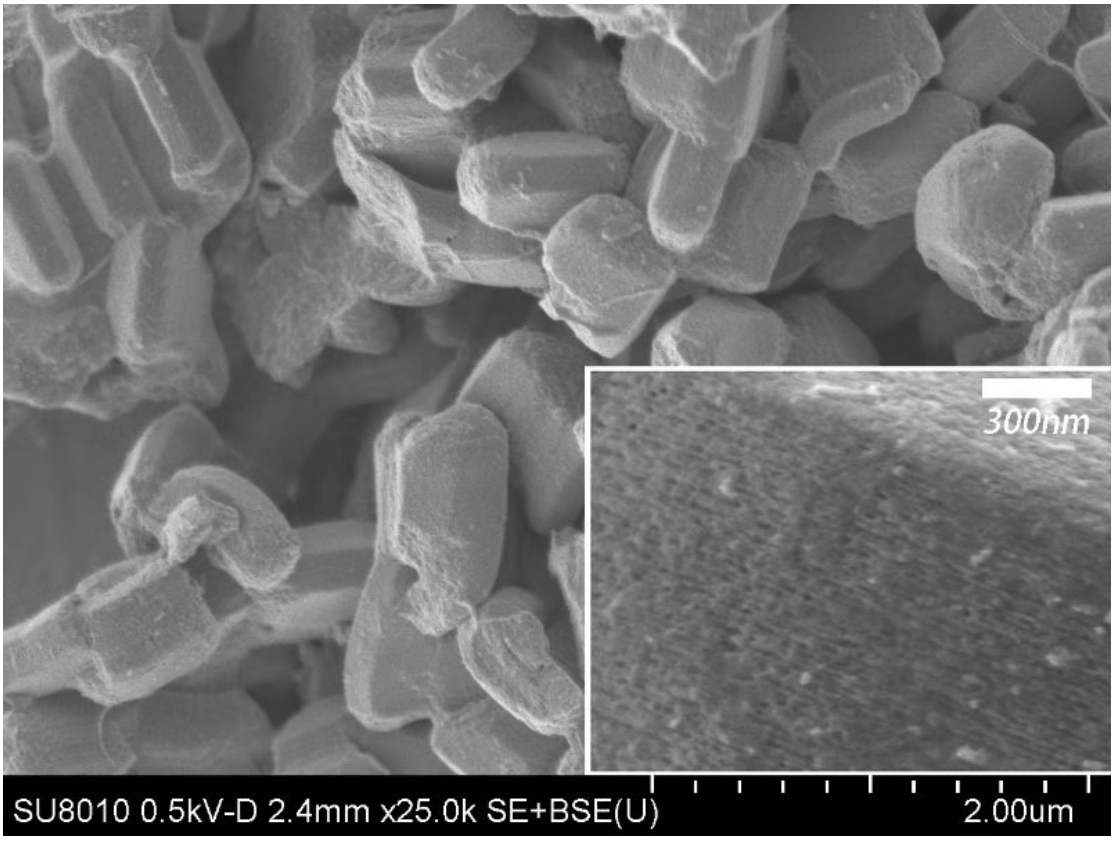

Fig. S-3 SEM image of CoPcF16-CMK-3/GCE.

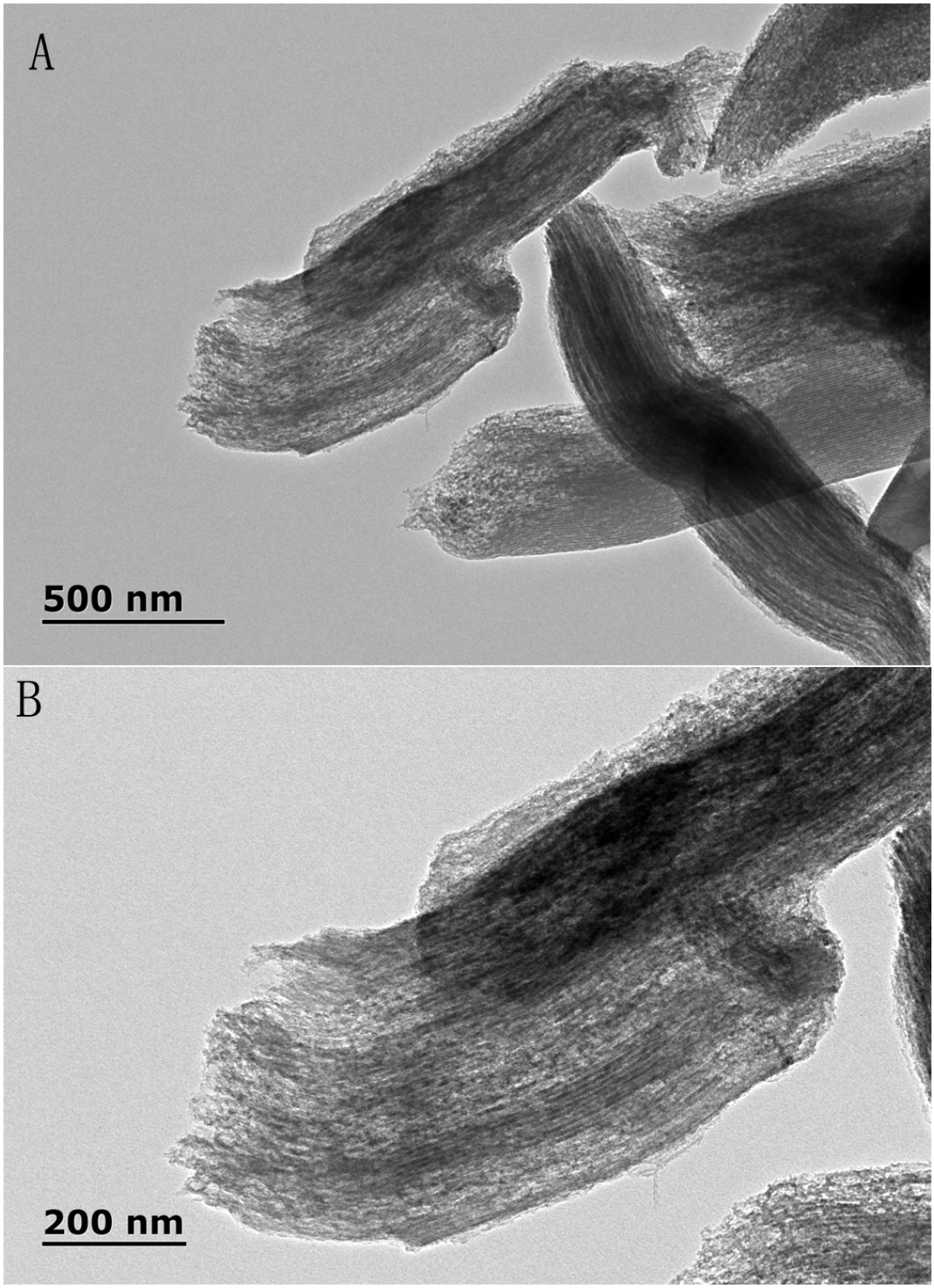

Fig. S-4 TEM images of CMK-3-CoPcF16.

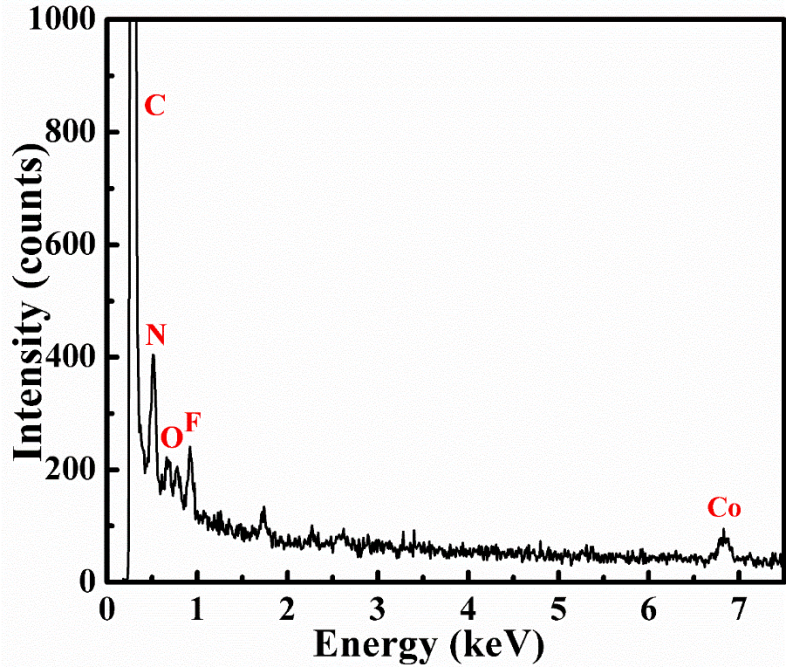

Fig. S-5 EDS spectra of CMK-3-CoPcF16

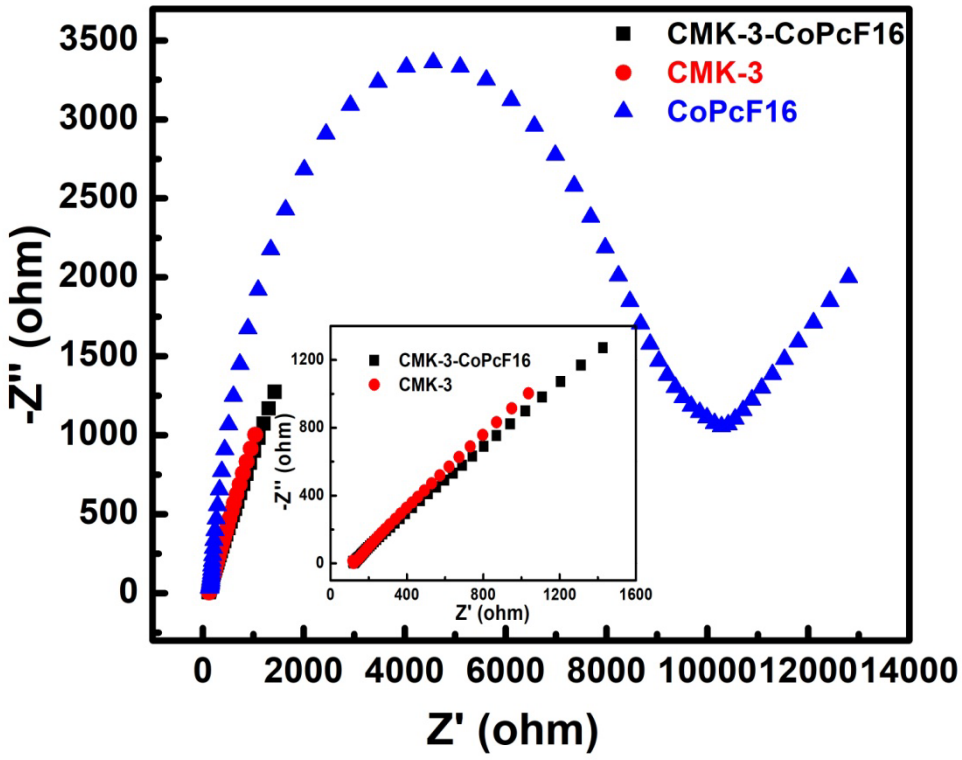

Fig. S-6 Nyquist diagrams for different modified electrodes in 5 mM [Fe(CN)6]3−/4− (1:1) solution containing 0.1 M KCl. The frequency range of EIS was in the range from 0.1 Hz to 100 kHz at 0.2 V.

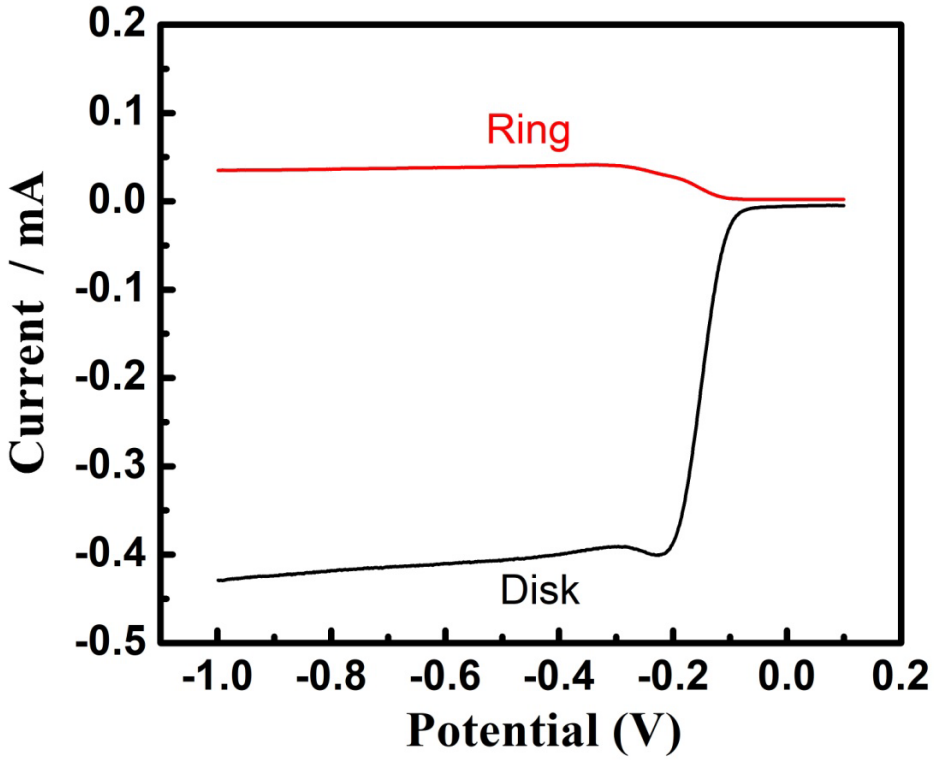

Fig. S-7 RRDE voltammetric curves of CMK-3-CoPcF16 in O_2-saturated 0.1 M NaOH solution under 1600 rpm with the scan rate of 5 mV/s and a Pt ring potential of 0.6 V.

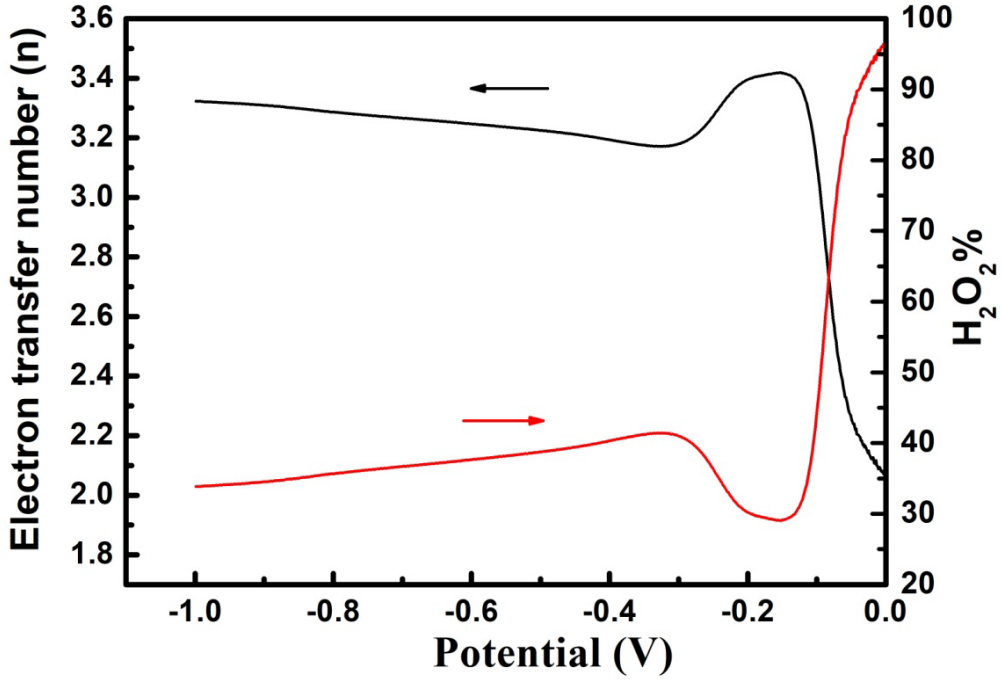

Fig. S-8 Calculated n and hydrogen peroxide yield (H_2O_2%) of CMK-3-CoPcF16 in ORR process from RRDE voltammograms.

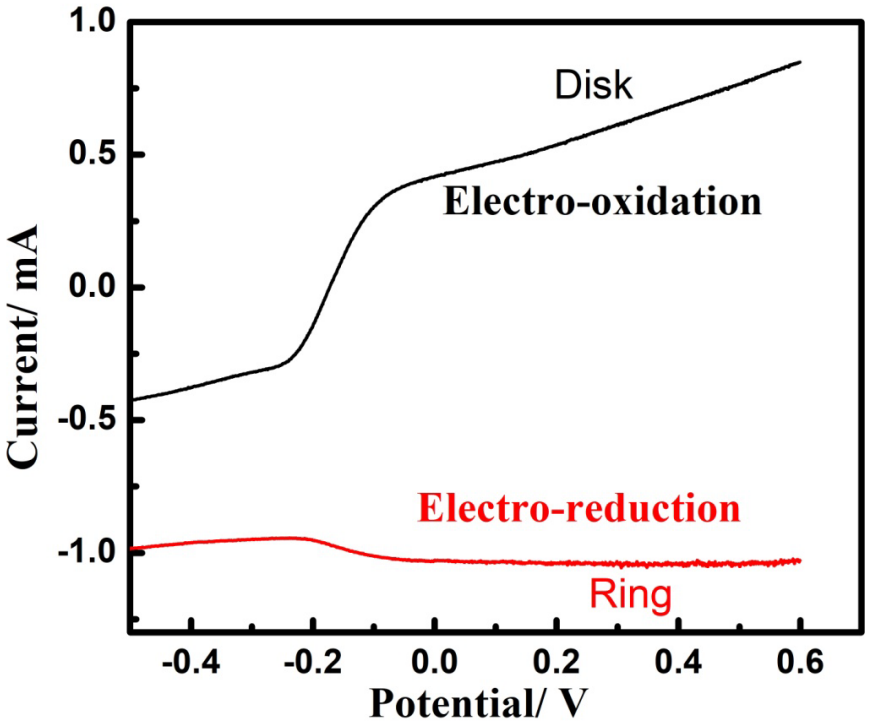

Fig. S-9 RRDE voltammetric curves of CMK-3-CoPcF16 in N_2-saturated 0.1 M NaOH solution in the presence of H_2O_2 under 1600 rpm with the scan rate of 5 mV/s and a Pt ring potential of -0.6 V.

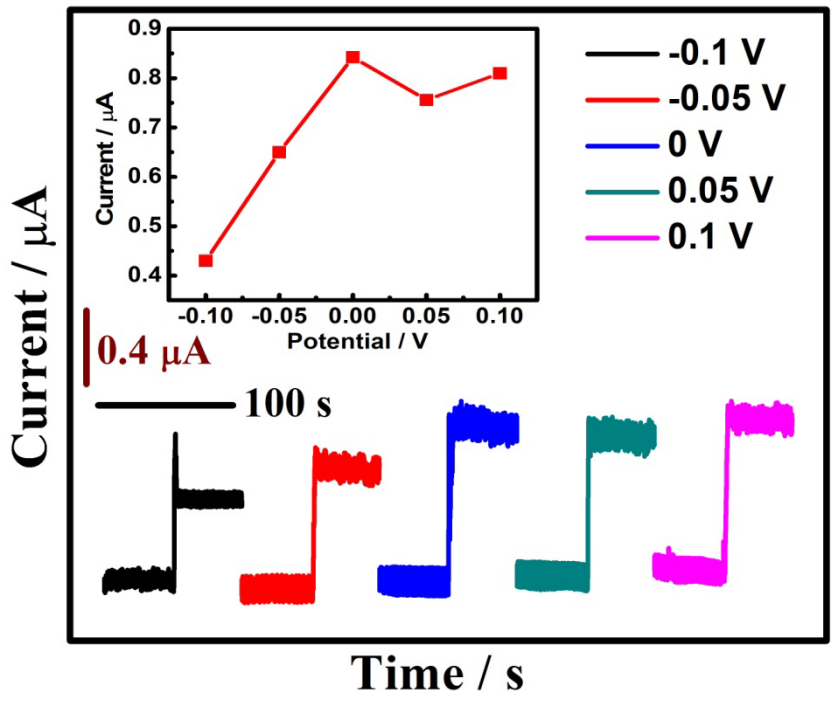

Fig. S-10 Effect of applied potential on the responses to H_2O_2

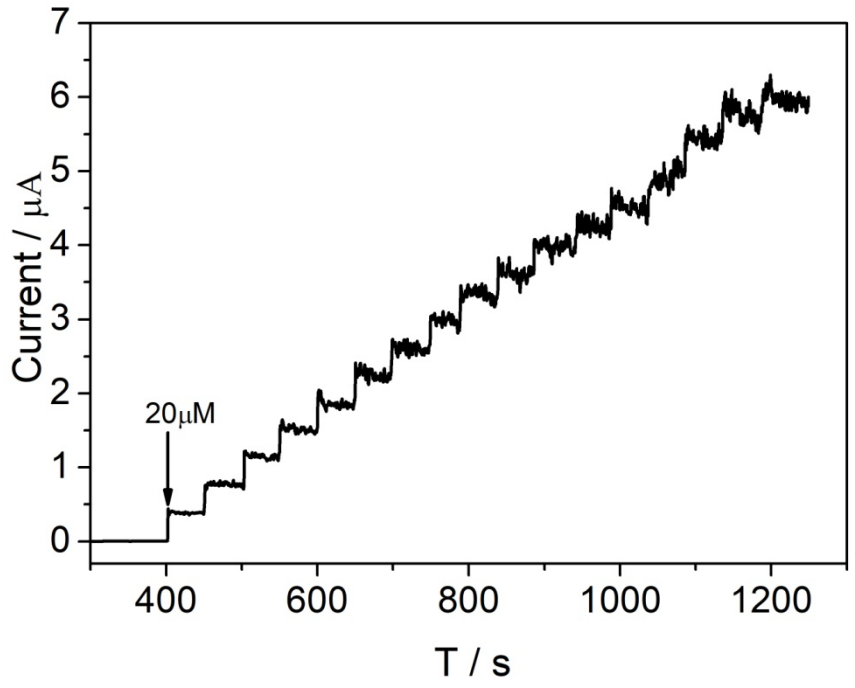

Fig. S-11 Repeatable response of CoPcF16-CMK-3/GCE to successive addition of H_2O_2 in stirred 0.1 M NaOH solution at an applied potential of 0 V.

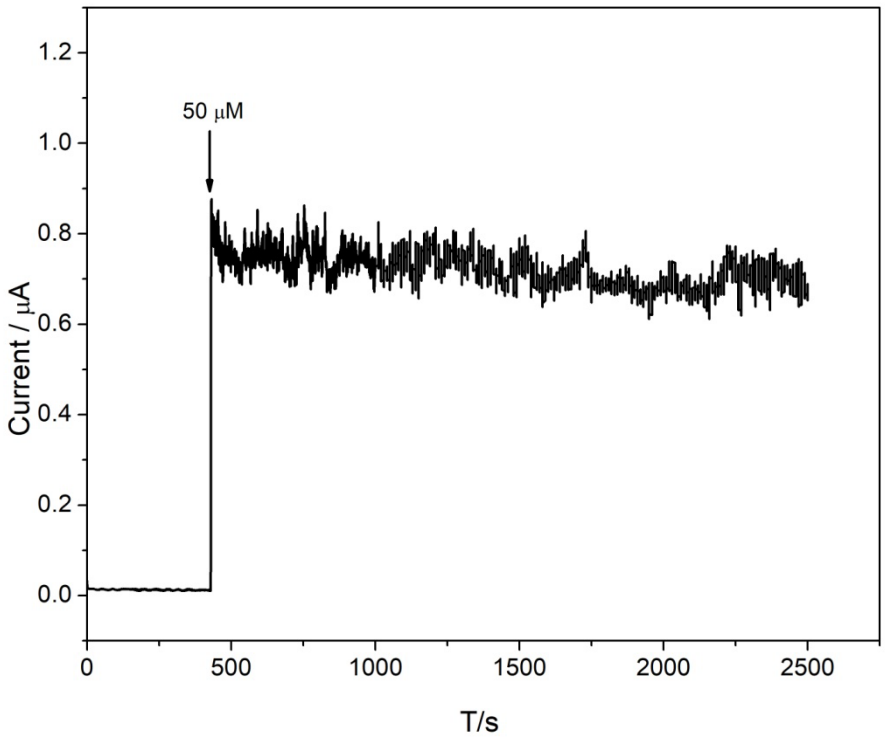

Fig. S-12 Long-term amperometric response of CoPcF16-CMK-3/GCE to 50 μM H_2O_2 in stirred 0.1 M NaOH solution.

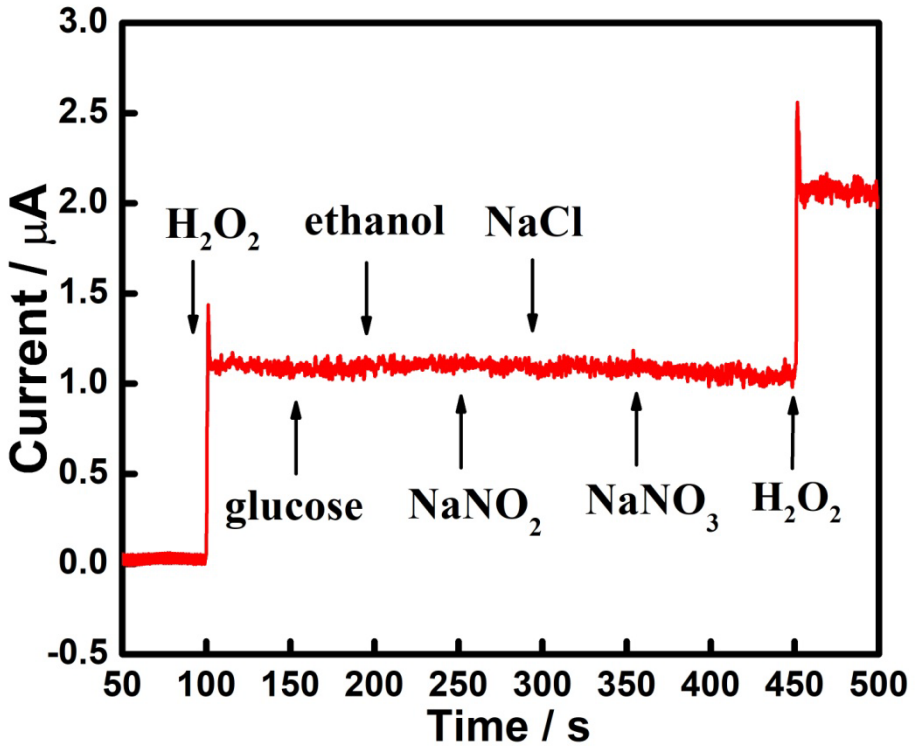

Fig. S-13 selectivity test of CoPcF16-CMK-3/GCE for H_2O_2 with addition of 10-folds concentration of glucose, ethanol, $NaNO_2$, NaCl, and $NaNO_3$, respectively.

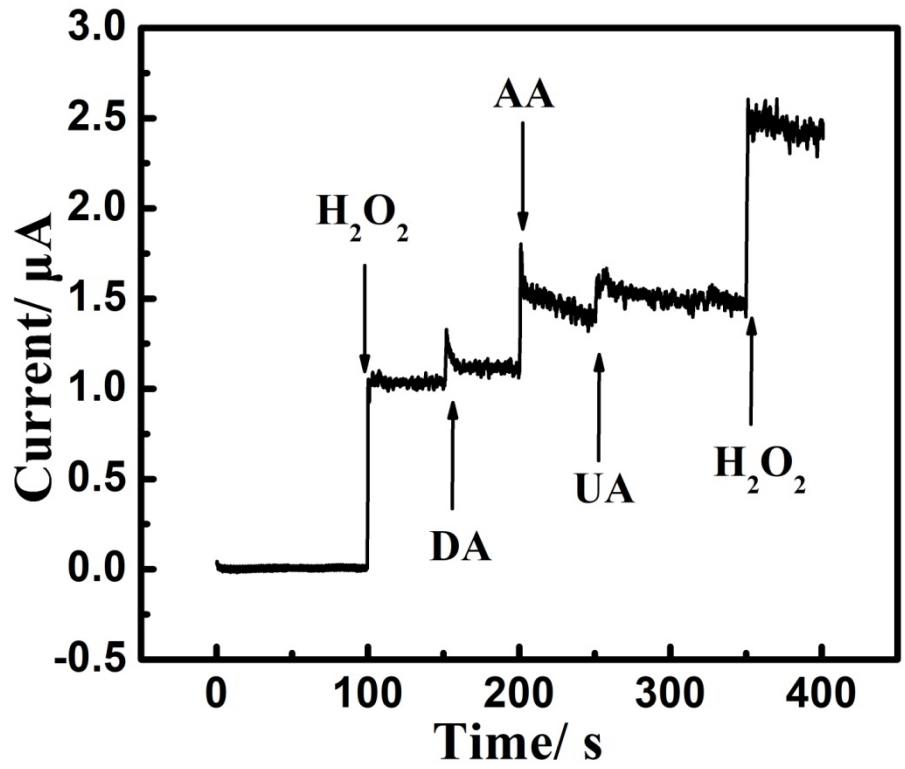

Fig. S-14 selectivity test of CoPcF16-CMK-3/GCE for 50 μM H_2O_2 with addition of 50 μM DA, 50 μM AA and 50 μM UA, respectively.

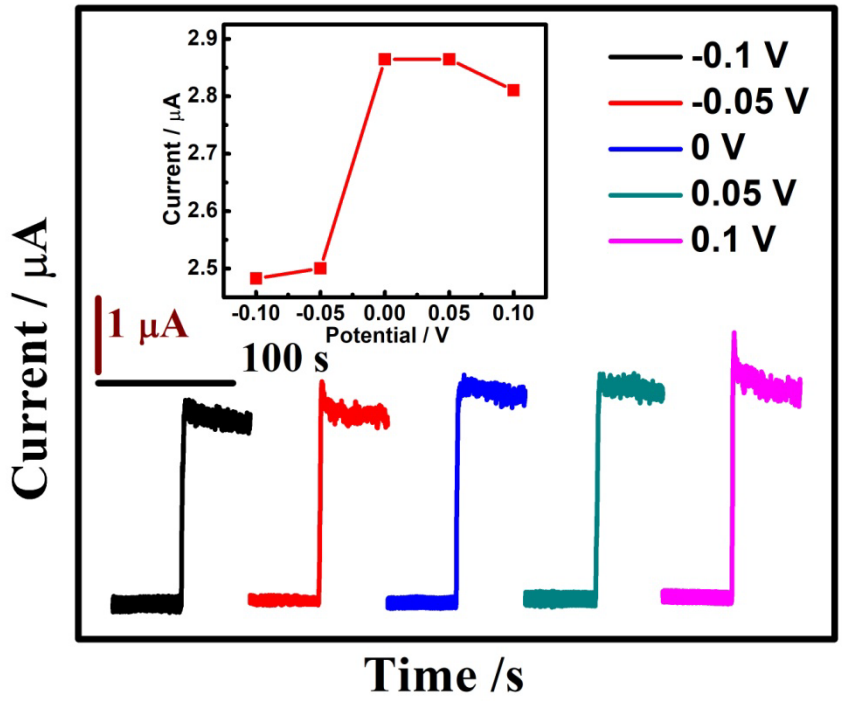

Fig. S-15 Effect of applied potential on the responses to hydrazine

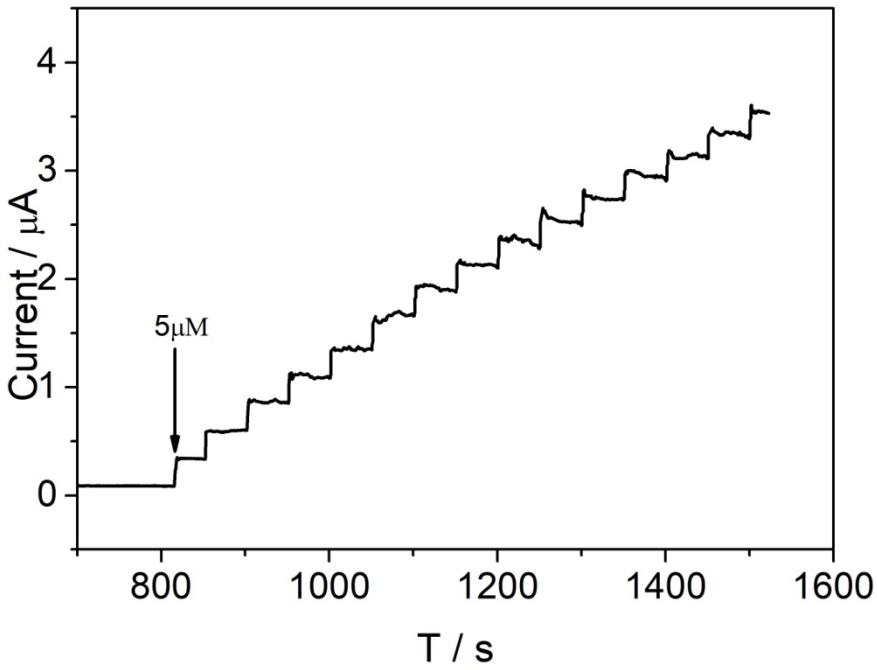

Fig. S-16 Repeatable response of CoPcF16-CMK-3/GCE to successive addition of hydrazine in stirred 0.1 M NaOH solution at an applied potential of 0 V.

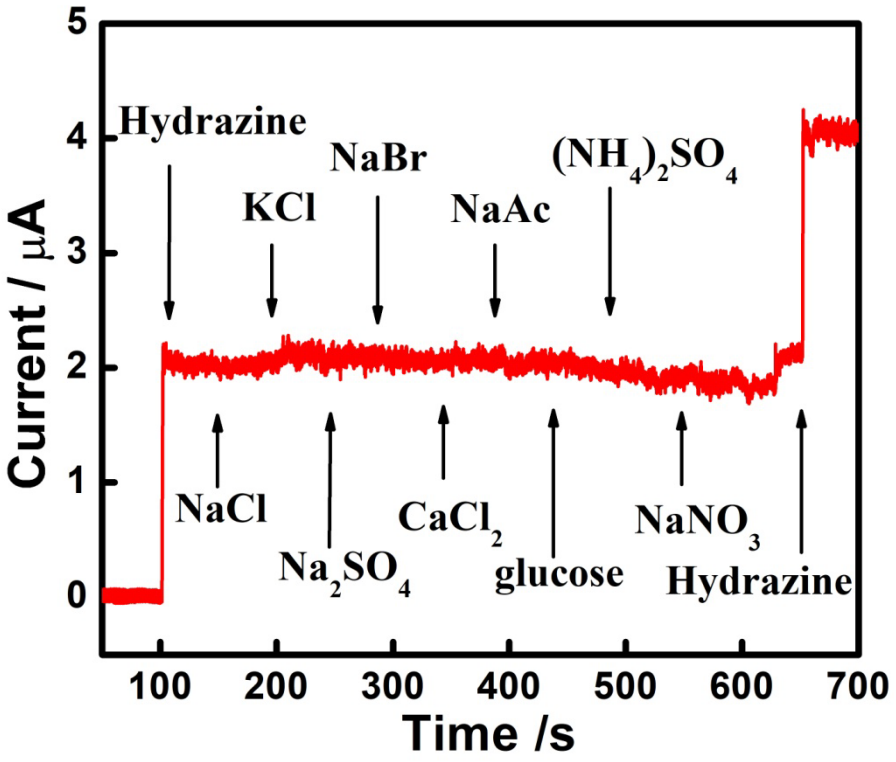

Fig. S-17 selectivity test of CoPcF16-CMK-3/GCE for hydrazine with addition of 10-folds concentration of NaCl, KCl, Na_2SO_4, NaBr, $CaCl_2$, NaAc, glucose, $(NH_4)_2SO_4$, and $NaNO_3$, respectively

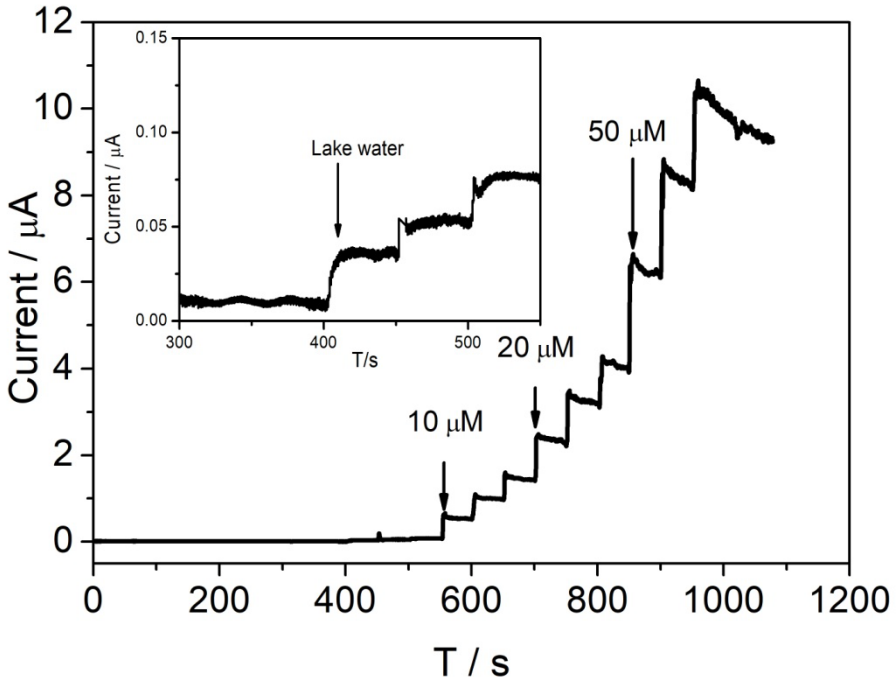

Fig. S-18 Applicability for the detection hydrazine in lake water

Table S-1. Sensing results for hydrazine in lake water

Added (μM)	Found (μM)	Recovery (%)	RSD (%)
10.0	10.3	103	2.9
20.0	19.2	96	3.3
50.0	45.2	90	4.6